A Deep Radio Survey of Abell 2125 II.

Accelerated Galaxy Evolution during a Cluster-Cluster Merger

Frazer N. Owen,[1,2], M. J. Ledlow[3,2,4], W. C. Keel,[5,2], Q. D. Wang[6], G. E. Morrison,[7,2]

ABSTRACT

Using our extensive radio, optical, near-IR and X-ray imaging and spectroscopy, we consider the reason for the unusually large number of radio detected galaxies, mostly found outside the cluster core, in Abell 2125($z = 0.2465$, richness class 4). With 20-cm VLA data, we detect continuum emission from 90 cluster members. The multiwavelength properties of these galaxies suggest that most of the radio emission is due to an enhanced star-formation rate. The dynamical study of Miller et al. (2004) suggests that Abell 2125 is undergoing a major cluster-cluster merger, with our view within 30 degrees of the merger axis and within 0.2 Gyr of core passage. The combination of projection effects and the physical processes at work during this special time in the cluster's evolution seem likely to be responsible for the unusual level of activity we see in the cluster. We argue that tidal effects on individual cluster members, often far from the cluster core, are responsible for the increased star formation. Our results are consistent with the idea that disk galaxies during this phase of a cluster's evolution undergo rapid evolution, through a burst of star formation, on their way to becoming S0's.

Subject headings: cosmology: observations — galaxies: evolution — galaxies: starburst — galaxies: elliptical and lenticular, cD — galaxies: clusters: individual (Abell 2125) — infrared: galaxies

---

[1]National Radio Astronomy Observatory, P. O. Box O, Socorro, NM 87801 USA.; fowen@nrao.edu The National Radio Astronomy Observatory is facility of the National Science Foundation operated under cooperative agreement by Associated Universities Inc.

[2]Visiting astronomer, Kitt Peak National Observatory, National Optical Astronomy Observatories, operated by AURA, Inc., under cooperative agreement with the National Science Foundation.

[3]Gemini Observatory, Southern Operations Center, AURA, Casilla 603, La Serena, Chile

[4]Deceased 5 June 2004. We shall miss his cheerfulness, unfailing good sense, and scientific industry.

[5]Dept. of Physics & Astronomy, University of Alabama, Tuscaloosa, AL 35487 USA

[6]Department of Astronomy, University of Massachusetts, 710 North Pleasant Street, MA 01003

[7]National Optical Astronomy Observatories, 950 N. Cherry Ave., Tucson, AZ 85719 USA

1. Introduction

With the recent convergence of supernova and CMB research to a remarkable consensus on the geometrical parameters of the universe, understanding the evolution of galaxies with cosmological epoch is, perhaps, the major goal of extragalactic astronomical research. From the morphology-density relation and the Butcher-Oemler effect, it is clear that the large-scale process of cluster formation must be a key part of the picture. But understanding galaxy evolution may be more difficult than geometric cosmology because of the complex role of dissipational processes, and the confusing results of observing two-dimensional projections of three dimensional physical objects (e.g. galaxies and clusters alike). Using as large a range of wavelengths as possible is one way to improve our understanding of what we are seeing. In this paper, we describe a study, using radio, optical, near-IR and X-ray imaging and spectroscopy, to try to understand how a very rich, very radio-active cluster, Abell 2125, fits into the bigger picture.

We began our study of the Abell 2125 field with moderately deep 20cm VLA C-array observations (Dwarakanath & Owen 1999; Owen et al. 1999). We compared Abell 2125 (a richness class 4, blue cluster at $z \sim 0.25$) with Abell 2645 (an apparently similar cluster at the same redshift but with much redder galaxies). We found a much higher detection rate of radio galaxies (27 vs 4) in Abell 2125, while the detection rate in A2645 is consistent with a normal AGN population in a lower redshift cluster. The excess in Abell 2125 occurs entirely in objects with $L_{20cm} < 10^{23}$ W Hz^{-1}, and thus seems consistent with a star-forming population (e.g. Condon, Cotton & Broderick 2002). However, only a small fraction of these radio-selected galaxies shows optical evidence of so much star formation, leaving the interpretation of the radio results in some doubt. Either the star formation in most of the low-luminosity radio sources is very well hidden at optical wavelengths, or we must seek some other explanation for the radio activity.

Closer examination of the optical and X-ray properties of Abell 2125 shows that it is not a typical, very rich Abell cluster. The galaxy distribution shows a central concentration together with an extension to the southwest, spanning at least 2 Mpc. X-ray observations (Wang, Connolly, & Brunner 1997) show the same pattern, and that the total X-ray luminosity is low for such a rich cluster. Wang, Connolly, & Brunner (1997) suggested that we might be seeing diffuse X-ray emission from a superstructure, as is seen in many cosmological simulations of large scale structure formation. Much of the excess radio-emitting galaxy population from Owen et al. (1999), like the diffuse X-ray emission, is contained in the southwest extension, not the cluster core. These factors suggest that the unusual galaxy population, especially as seen at radio frequencies, might be connected to the large-scale nature of Abell 2125 itself.

To study this cluster further, we have made much deeper and higher resolution radio observations using all four VLA configurations. These deep radio data have also motivated deep optical and NIR imaging, optical spectroscopy, deep submillimeter observations, and a long *Chandra* exposure. While some of these ancillary observations were motivated by possibility of studying a background sample, we consider here what they tell us about Abell 2125.

Paper I (Owen et al 2004a) described our radio, optical and NIR observational program to study the region of the sky centered on Abell 2125. In this paper, we now discuss the properties of the cluster members, particularly in light of the unusually large number of radio detections from cluster's members. Physical quantities are calculated using a WMAP ΛCDM cosmology with H_0=71 km s^{-1} Mpc^{-1}, $\Omega_M = 0.27$ and $\Omega_V = 0.73$.

2. Observations

2.1. Ground-based and X-ray Imaging and Spectroscopy

Most of the observations and reductions have been described elsewhere. The radio, optical and near IR imaging and reduction is described in paper I (Owen et al 2004a). The optical spectroscopy is discussed in (Miller et al. 2004). The *Chandra* imaging, reductions and basic results are presented in (Wang, Owen & Ledlow 2004).

2.2. HST Imaging

We observed three fields in Abell 2125 with HST and WFPC2, centered to maximize the number of radio-detected members within the fields without imposing tight orientation constraints. One field is just west of the cluster core, with the other two spanning the clump of bright galaxies 5' SW of the center. Each of these latter two fields was observed twice; for the southwest field, at significantly different orientation angles, and for the southern field, at pointings differing by about 10 arcseconds. Both F606W and F814W filters were used, corresponding roughly to the emitted B and R bands at $z = 0.2465$. Each filter was used for an exposure of 2600 seconds per observation, split into two equal parts for cosmic-ray rejection.

Several of the images were taken at small angles to the illuminated limb of the Earth, and suffered from scattered Earthlight. This produces a diagonal X pattern of brighter regions. These were removed following the same basic precepts as used for the original

Hubble Deep Field data (Williams et al. 1996). Where multiple pointings with similar scattering properties were available, they were combined to reject actual objects, then scaled to a common scattering intensity and smoothed. This scattering model was applied, with appropriate scaling, to all the affected images. Since this procedure does not necessarily preserve mean sky brightness as it affects photometric errors, nor impose a consistent sky level across the various CCD fields, we added a constant value to give the same level for all chips.

3. Results

In Table 1, we present our basic observational results for spectroscopically confirmed, radio detected members of Abell 2125. In column 1 we list radio source name; columns 2 and 3 contain the optical R.A. and Declination (2000.0) corresponding to the galaxy (for members identified with radio emission detected at $> 5\sigma$ above the noise). Column 4 contains the distance in arcmin from the nominal cluster center [15 41 15, 66 16 00] (Owen et al. 1999). In columns 5 and 6, we list the peak and total flux density for each radio source in μJy. Column 7 contains the size (or a limit) in arcsec. If the source is resolved and fitted with a two dimensional Gaussian, we give the deconvolved major axis size (FWHM), the minor axis size and the position angle. If only a size is given, this value has been estimated from the image by hand. Column 8 lists our best measured value for the redshift; an "e" indicates that emission lines were present in the spectrum (Miller et al. 2004).

3.1. Photometric Analysis

We have quantified the spectral energy distribution ,SED, of each radio galaxy, using the publicly-available program *hyperz* (Bolzonella, Miralles, & Pelló 2000) to fit template spectra. We measured optical magnitudes for each of our 10 bands from U to K in the Gunn-Oke aperture (radius 13.1 kpc). In table 3, we give AB magnitudes used for the *hyperz* results quoted. -9.00 in table 3 indicates no measurement was available. Then *hyperz* was used, with the redshift range constrained to fall within the cluster range in light of the spectroscopic redshifts, to fit the Bruzual-Charlot models provided with the program (GISSEL98; Bruzual & Charlot 1993) with a Calzetti extinction law (Calzetti et al. 2000) and with a total age less than the age of the universe at $z = 0.2465$, about 10.8 Gyr. The result yields a spectroscopic "galaxy type", an age for the dominant star-forming event, an A_V extinction for the Calzetti law, and a rest-frame, R absolute magnitude. In table 2, we summarize the model star-formation histories used. The galaxy type is based on an assumed

e-folding timescale for the star formation. This timescale, combined with the age assigned to each template, determines each SED in the catalog. For ages which are a significant fraction of a Hubble time, templates for different galaxy types may not differ very much. It is not clear that the galaxy type assigned to each e-folding timescale is closely correlated with the galaxy morphology. Finally, the galaxy ages are a (luminosity-weighted) global estimate for the stars in the aperture and may not reflect the age of the star-formation event which we are observing in the radio. Thus we prefer to look on the types as a way of parameterizing the catalog with a useful range of assumed star-formation histories. The dominant parameter in a template is the age of the assumed stellar population, especially for ages of a Gyr or less. The extinction is a useful dimension to explore and seems generally correlated with star-formation, although derived age and extinction are somewhat anti-correlated. The absolute magnitude should be robust, since we are essentially using *hyperz* to interpolate between our measured magnitudes using the best fitting SED.

3.2. Emission Lines

Another important clue to the nature of radio population is the detection (or lack) of emission lines. Our spectroscopy comes from several different observing runs with different wavelength ranges covered. Thus we cannot report a common set of emission lines. However, in almost all cases, we detect [OII] and/or Hα/[NII]. Often [OIII], Hβ and [SII] are detected. As reported in Miller et al. (2004), almost all the galaxies with detected emission lines have line ratios indicating that they are powered by star formation. Of course, for very powerful AGNs, one expects to see a rich spectrum of broad and/or narrow lines. However, at the radio luminosities and redshift we are dealing with, one rarely can detect emission lines in contrast against the stellar continuum (Owen, Ledlow, & Keel 1995). Thus for the relatively low-luminosity radio objects we are observing, the lack of detected emission lines together with detected radio emission is consistent with (weak) AGN activity. However, the lack of emission lines can also be consistent with significant star formation if dust obscures the line emission (Miller & Owen 2002). Thus when we see line emission in these systems, that result normally indicates star-formation activity as the origin of the radio emission. However, for the galaxies in which we do not detect line emission, the situation is less clear.

3.3. Physical Parameters

In table 4 we summarize the physical parameters for each galaxy with radio emission. All values have been calculated assuming a redshift of 0.2465 (Miller et al. 2004). Column

1 contains the source name; column 2, the largest linear size; column 3, the absolute radio luminosity; column 4, the projected distance from the cluster center; column 5, the absolute, rest frame R magnitude, column 6, 7 and 8, the *hyperz* results: spectral type (table 2), age and A_V, and column 9, the spectroscopic redshift. Once again an "e" appended to the redshift indicates emission lines are detected.

3.4. *Chandra* Detections of Cluster Members

Compact X-ray sources in galaxies are usually associated with active galactic nuclei (AGN). Our *Chandra* data for Abell 2125 reach flux levels at which star-forming galaxies can also be detected (Ranalli, Comastri, & Setti 2003). On the other hand, detection of X-ray emission on larger scales than galaxies is usually associated with free-free emission from the hot cluster medium. Thus one major goal of the *Chandra* observation was to use X-ray detections of compact emission from the individual galaxies with radio emission to recognize AGN. If a large fraction of the radio activity was driven by AGN, even in emission-line galaxies, we might expect to detect a large fraction of the radio-emitting cluster members. The *Chandra* observation shows 99 discrete sources, as detailed in Wang, Owen & Ledlow (2004).

Eight radio-detected galaxies in Abell 2125 also host point-like X-ray sources independently detected from the *Chandra* observation (table 5). One of these sources, 00047 (also called C153) shows unique extended structure on close inspection, as discussed in detail in our paper on the cluster core (Owen et al 2004b). However, the low background level of the *Chandra* detectors allows deeper detections of sources if the positions are independently and accurately known; using the optical positions to fix locations of potential X-ray sources yields an additional twelve X-ray detections with probabilities $< 10^{-3}$ of being random events. The true probability of these weaker detections being spurious was further evaluated by shuffling the coordinates of the galaxies and repeating the search. These tests indicated that ~ 0.8 detections could be expected by chance for the entire radio galaxy sample from this procedure. The errors on the fluxes are large for these detections and there is a statistical bias to overestimate the fluxes by as much as a factor of two (Wang 2004). Thus the luminosities quoted should be taken only as very rough estimates. These additional 12 faint X-ray detections are listed in table 6. Once again one of the radio detections (00057) is clearly extended in X-ray emission, associated with one of members of the central triple in the cluster core (although it is not detected by the point source detection algorithm used by Wang (2004)). This galaxy is also discussed in Owen et al (2004b).

In table 7 we list two other cluster members which are associated X-ray sources reported by Wang, Owen & Ledlow (2004). Neither of these galaxies has detected emission lines. However, one (X072) also has a marginal radio detection, with a peak between 3–4 σ on the radio image. The other source (X064), associated with a cD-like galaxy, is also extended and soft.

The new X-ray analysis brings the detected fraction among radio-selected cluster members to 20/73, within the region covered by the *Chandra* image. Excluding the very extended sources in the cluster core, all the detections by Wang, Owen & Ledlow (2004) are associated with relatively bright galaxies ($M_R \leq -22.0$) without emission lines. Three of the weaker X-ray objects from table 6 also lack emission lines and only one is fainter than $M_R = -22.4$ (i.e. -21.8). All of these objects seem consistent with AGN. Furthermore, the X-ray morphology of five of the additional, weaker objects associated with emission lines (and one without emission lines) are not clearly point-like (at 6 arcsec or 23 kpc resolution); therefore these X-ray sources are large with respect to the galaxy scale and these galaxies may simply be confused with a local peak in the extended X-ray emission. Thus it is hard to evaluate the origin of the the X-ray detections for these objects. Only three of the weaker galaxies with emission lines do appear point-like. These objects (00022, 00026 and 00027) are associated with relatively radio-luminous objects consistent with star formation. The X-ray luminosities of these objects also are consistent with star formation at the same general level as implied by the radio emission within the errors (Ranalli, Comastri, & Setti 2003).

In summary, 53/73 radio-detected galaxies in the *Chandra* field are *not* detected in X-rays. Ten of the X-ray-detected objects are consistent in optical, radio, and X-ray properties with AGN. Three others are most consistent with star formation strong enough for X-ray detection. The rest are either associated with diffuse emission, or are too weak and/or in regions too complex to characterize clearly. Thus the *Chandra* data do not suggest that the bulk of the radio activity is due to AGN.

3.5. Radio Luminosity/Morphology

Statistically, 10^{23} W Hz^{-1} is the approximate crossing point of the luminosity functions of radio galaxies driven by AGN and star formation. Above 10^{23} W Hz^{-1} AGN dominate, below 10^{23} W Hz^{-1} star-forming galaxies dominate (Condon, Cotton & Broderick 2002). In rich clusters, where there are more early-type galaxies, the log of the crossover luminosity is nearer 22.8 (Miller & Owen 2002). However there are, of course, objects above and below the crossover luminosity driven by the non-prevailing mechanism. Thus radio luminosity is a *statistical* indicator of AGN or star-formation-driven radio emission.

Radio morphology is another important indicator. Clear, FR I or FR II morphology is a clear AGN indicator. Most of the sources with radio luminosities above 10^{23} W Hz^{-1} in A2125 show clear FR I or FR II morphology (Dwarakanath & Owen 1999).

3.6. Radio/Optical Alignment

Beyond source luminosity, another important indicator that radio emission is driven by star formation is alignment of radio emission with the major axis of a galaxy. While star formation in some systems is too concentrated in the galaxy core to resolve at our 1.5" (5.7 kpc) limit, extended and aligned radio emission is a strong clue that the emission is driven by star formation.

A large fraction of the lower-luminosity sources show alignment between the radio and optical structures. In figure 1 we show radio contour maps overlaid on the MOSAIC R-band optical images as examples of the aligned structures. However, some of the radio cluster members show other features which are not aligned. In many cases, both aligned and misaligned radio structure can be seen. In some cases only misaligned structures are seen. In figure 2 we show some of these misaligned features. Some of the misaligned radio features could represent outflows directed along the minor axis, either the jets of AGN, or starburst-driven winds (Colbert et al. 1996). In some cases, these features could be evidence of on-going stripping of the galaxy's ISM as it moves relative to the external medium.

3.7. Concentration Indices

Optical morphology is another important clue to understanding what we are seeing in galaxies. However, except in the small regions imaged with HST, the resolution of our optical imaging, is too low for detailed classification. We therefore quantify the morphological types spanned by the radio galaxy sample using concentration indices measured for 81/90 of the sources. No reliable measures were obtained for the other 9 galaxies due to the proximity of brighter companions or very bright stars.

We measure the concentration index (similar to a bulge-to-disk ratio), defined as the ratio of the flux between inner and outer isophotes, where the outer isophote is measured to 24.75 magnitudes arcsec^{-2} in the rest-frame of the galaxy. The inner isophote is normalized to 0.3 times the radius of the outer isophote. While our imaging is sufficiently deep to extend to fainter limiting surface-brightness (Abraham et al. (1994) used 25.5 mag arcsec^{-2}), the majority of the radio galaxies in A2125 are in high galaxy-density regions, many with close companions, making it difficult to separate overlapping isophotes. The 24.75 mag arcsec^{-2} limit was a compromise which allowed us, with masking, to fit nearly all the galaxies to a uniform depth. The difference in CI measure with different surface-brightness limits is fairly small (of order 0.02-0.03), which is an estimate of the typical error bars.

In figure 3 we plot the concentration index versus mean surface-brightness for 81 cluster radio galaxies. The upper dotted line shows the expected location of galaxies with $r^{1/4}$ laws, while exponential disks are plotted with a solid line. There is clearly a spread in values, with a substantial (30/81, 37%) fraction falling intermediate between bulge and disk-dominated profiles, as would be characteristic of an S0 classification. The open circles in figure 3 indicate objects in which the SFI, discussed in the next section, suggests little or no evidence of star-formation based on a number of indicators. The solid symbols indicate some evidence of star formation based on SFI. Clearly most of the objects near the $r^{1/4}$ law line are consistent with old stellar populations while most of the points below this line show some evidence for star formation.

3.8. Star formation or AGN ?

One of the major questions raised by the galaxy population in Abell 2125 is whether the excess radio emission is due to star-formation or nuclear activity. As discussed in section 3.4, the X-ray results, perhaps the most robust single tracer of AGN. show that less than 15% of the radio sample appear to be AGN. As discussed in Owen et al. (1999), for cluster of this richness, there is no excess in the radio-galaxy population above 10^{23} W Hz^{-1} where radio AGN normally dominate. However, many of the optical identifications below 10^{23} W Hz^{-1} do not show the obvious colors and emission lines one might expect from star-bursting galaxies. For galaxies at the distance of Abell 2125, mainly observed from the ground, any given star-formation indicator may or may not be detectable depending on the details of an individual galaxy's properties. With the relatively coarse spatial sampling used for optical imaging and spectroscopy, much of the light from a massive galaxy may come from its old stellar population. The orientation and dust content will also affect the emission line equivalent widths and the effective age of the SED. For systems close to edge-on, the radio emission from star formation is expected to align with the galaxy disk, if it is resolved. But for a face-on system, this alignment is harder to detect. In practice, we need to look at several different indicators to understand the likely origin of the radio emission.

With our new dataset, much larger than used in Owen et al. (1999), we can look for evidence of star formation in several different ways. Indicators we can use include: 1) radio luminosity, 2) radio alignment with optical galaxy major axis, 3) optical emission-lines,

4) optical/NIR SED, 5) dust A_V required by the best fit SED, 6) absolute R-magnitude. We calculate a weighted "star-formation index" (SFI) for each galaxy to give us an overall indication of the likelihood of star formation being responsible for the radio emission. Some indicators seem better than others, so we will assign weights of 0.5 or 1.0 for each of the six properties depending on how good the evidence seems to be. Radio alignment and emission lines seem to be particularly good indicators, so each of these is worth 1.0 in our scheme. Radio luminosity is only a statistical indicator and in clusters, is really only a strong one when $\log(L_{20cm}) < 22.7$, so we add 0.5 in this case. Likewise, Ledlow & Owen (1996) and Miller (2001) show that AGN in clusters are rarely if ever more than one magnitude fainter than L_*. This limit corresponds to $M_R = -21.0$ for our magnitude system. We will add 0.5 to the score for M_R fainter than -21.0. Likewise most AGN are associated with old stellar populations and even strongly star-forming galaxies can appear to have relatively old SEDs. Thus we will add 0.5 to the score if the age of the best fit SED is < 5 Gyrs and 1.0 if it is < 1 Gyr. Finally, dust correlates with star formation. We will add 0.5 for an $A_V > 0.5$ and 1.0 for $A_V > 1.0$. Thus the maximum score in this system is 5.0.

Table 8 summarizes the SFI scores for the 90 galaxies with radio detections. Only one galaxy has a perfect 5.0 rating, while 21/90 have SFI < 1. These seem likely to be AGN. Fifteen have intermediate SFI of 1 or 1.5. These systems are consistent with star-formation but are not as certain as galaxies with higher SFI. The 54 with SFI of 2 or more and seem likely to have radio emission driven by star formation. This comparison of multiwavelength indicators suggests that most of the excess activity in Abell 2125 is driven by star formation.

In figure 4, we plot of the radio luminosity versus the absolute R magnitude. The solid symbols show which galaxies had detectable line emission; the squares show which galaxies had aligned radio and optical emission. We believe these two indicators are the best for signifying star formation. Figure 4 suggests a break point in the galaxy properties at $M_R = -22.3$. No galaxies brighter than $M_R = -22.3$ show evidence of star formation, while most of the galaxies fainter than this show emission lines and/or radio alignment. Several of the remaining objects fainter than $M_R = -22.3$ also show dusty SEDs suggesting that we may be losing the emission-line spectra to dust extinction.

In figure 5 we show histograms of the radio linear size distributions for the aligned sources (left panel) and the sources with radio emission without clear alignment (right panel, in which upper limits are shown in black). Most of the emission-line objects which show alignment (left panel) have rather extended radio emission, much larger than the galaxy core. Thus we seem to be seeing extensive star formation throughout disks of most of these systems. Most of the emission-line galaxies without clear alignment (right panel) have a much smaller radio extent. Over half only have upper limits to the radio size. These latter objects appear to be consistent with more compact star-formation events. All these objects seem to be consistent with star formation as the origin of the radio emission.

Thus there is a strong tendency for the optically and radio fainter galaxies to be consistent with star formation as the origin of the radio emission. Also, by number, most of the radio-emitting galaxies we have detected are most consistent with star formation, but almost all galaxies more than 30% brighter than L_* are consistent with AGN activity.

In figure 6 we show the histogram for all the absolute radio luminosities. The black boxes indicate objects with M_R brighter than -22.3. In figure 6 one can see the lower cutoff in 20cm radio luminosity, $\log L_R$, at 21.6 and the peak in detections near 22.3. Also one can see the tendency for the optically brighter galaxies to dominate the sample above $\log L_R > 22.8$, where one would expect AGNs to dominate as discussed earlier. The drop-off in numbers at faint levels probably combines several effects. First, away from the field center the sensitivity drops off. Second, extended sources at near the point source limit will be missed. Third, a few faint objects with fainter optical IDs still do not have redshifts and could be cluster members. Thus it seems premature to conclude the the true radio detection rate in the cluster peaks at $\log L_R > 22$. A deeper radio survey would likely detect many more star-forming systems and there is a large population with emission lines in Miller et al. (2004) which have not yet been detected in the radio.

To estimate a SFR implied by the radio luminosities, we can use the calibration of Yun, Reddy, & Condon (2001), who used the radio-FIR correlation to estimate the radio-SFR relation. Yun, Reddy, & Condon (2001) estimate the SFR assuming a Salpeter IMF down to 0.1 $M_\odot$. In order to include only star formation above 5 $M_\odot$, we scale their relation by 0.18, and, corrected to our assumed cosmology, the result is

$$SFR(M_\odot yr^{-1}) = 1.0 \times 10^{-22} L_R(WHz^{-1}). \tag{1}$$

Thus our peak near $\log L_R = 22.3$, corresponds to about a SFR of about 2 $M_\odot yr^{-1}$ (or 11 $M_\odot yr^{-1}$ for a Salpeter IMF down to 0.1 $M_\odot$). Mostly these galaxies appear to exhibit relatively modest rates of star-formation.

As discussed earlier, while most of the X-ray detections are most consistent with AGN or diffuse X-ray emission in the local area surrounding the detections, three of the radio galaxies have weak point-like X-ray emission. Ranalli, Comastri, & Setti (2003) have shown that the X-ray luminosity in star-forming galaxies also correlates with the SFR. Converting their results to our cosmology and to the 0.5-8 keV band, assuming a photon number index of 2 (Wang, Owen & Ledlow 2004), we get

$$SFR(M_{\odot}yr^{-1}) = 6.8 \times 10^{-41} L_{0.5-8keV}. \quad (2)$$

From equation 1 and the data on the only three radio detected galaxies in table 6, one gets radio SFR estimates of 3.2, 3.5 and 5.2 $M_{\odot}yr^{-1}$ for 00022, 00026 and 00027, respectively. From equation 2 the estimates from the detected X-rays for the same three objects are 6.3, 14 and 14 $M_{\odot}yr^{-1}$, respectively. Given that the X-ray measurements are biased high, that we are just marginally able to detect the X-rays from the galaxies with the highest SFR's and that there is significant scatter in the radio/X-ray correlation (Ranalli, Comastri, & Setti 2003), the agreement in the SFR estimates from both bands is consistent with a star-formation origin to both the radio and X-ray emission for these three objects.

3.9. HST Images of Radio Galaxies

Figure 7 shows images of radio galaxies from the HST observations. The images are true color in the sense that red represents redder light and blue bluer light from our V and I images. In the bottom two cases, we overlay the contours of radio emission. These galaxies give some insight into what the ground-based observations are telling us about the population as a whole.

Object 18033 has an SED which *hyperz* fits with an old Sb. The HST morphology fits with this Hubble type. The galaxy has emission lines and aligned radio emission. It has a radio SFR of about 6 $M_{\odot}yr^{-1}$. The size of the radio source is only about 8 kpc (2 arcsec), about the size of the redder region in the galaxy core, which may indicate dust obscuration of much of the star-forming region.

Galaxy 24015 is best fit by an "elliptical" SED but with an age of only 4.5 Gyr. However, the region fitted by *hyperz* is interior to the the spiral arms seen with HST. The radio emission is aligned and consistent with a star-formation rate of 2 $M_{\odot}yr^{-1}$.

Galaxy 24030 (on the east side of image) is also fit by a young "elliptical" SED but shows all the other indications of star-formation at a modest rate. A close look at the HST image suggests spiral structure.

Object 24027 (in the center of the image) is fit by a burst model of the same age as 24030 (4.5 Gyr). It shows little evidence for star formation except for an A_V of 0.6. The HST image has a red core also suggesting dust obscuration. The radio source to the north and west of 24027 appears to be unrelated since it is coincident with a very faint object on the HST image; there is a faint *Chandra* source at that position.

Object 24016 has an SED best fit by an old "S0" with some dust. This is consistent with the red core and the lack of emission lines. However, the radio emission appears quite extended and the NE lobe of the radio source is coincident with a very blue object. This blue object also shows strong [O II] emission in our narrow-band image. Since this object is outside the region covered by the optical spectroscopy it is hard to guess what is going on here, whether a superposition of an unrelated late-type galaxy or some sort of jet-induced star formation. This main galaxy is still most consistent with an old stellar population and AGN, but would require more study to understand the pattern we see.

Overall, the HST imaging supports the conclusions drawn from the ground-based observations. However, the galaxy types provided by *hyperz* through the Bruzual-Charlot templates, need to be taken with a grain of salt and only used as a general guide to the nature of each galaxy in the region covered by the aperture used for the photometry. Many of the objects do show morphological evidence for dusty cores as well as from the SED fitting.

3.10. Location of Activity in the Cluster

One of the important clues to understanding Abell 2125 is the location of the radio galaxies with respect to the nominal cluster core and the diffuse X-ray emission. In figure 8 we show the histogram of the projected distance from the nominal cluster center for the radio cluster members. The black boxes indicate sources for which $SFI < 1$, the most likely AGN. Clearly most of the radio emitters are fairly far from the cluster core, compared with the core radius from *Chandra* of ~ 250 kpc (Wang, Owen & Ledlow 2004).

Three of the radio luminous objects are associated with the triple system in the center of the cluster core and have SFI=0. Excluding these objects, both the likely AGN and the entire sample have median projected distances from the cluster core of ~ 1.3 Mpc. Thus most of the radio detections, AGN and star-forming galaxies alike, lie far outside the cluster core.

Wang, Owen & Ledlow (2004) present the X-ray results for imaging of the diffuse structure in Abell 2125. The diffuse X-ray structure of Abell 2125 gives a picture of a relatively cool, moderately low luminosity system, $\sim 10^{44}$ erg s^{-1}. The main cluster concentration has a temperature near 3 keV, while the more diffuse structures to the SW have $T \sim 1$ keV. From Wang, Owen & Ledlow (2004) one can see that this extremely optically rich cluster (R=4) is not a particularly impressive X-ray cluster. Its luminosity, temperature and density are more like a much lower-richness cluster. Furthermore, the lower surface brightness regions outside the bright core are significantly cooler. The full size of the X-ray emitting region is at least 4.5×2.2 Mpc in projection, centered SW of the core by about 1.2 Mpc.

In figure 9 we mark the radio emitters on the optical field. Objects in red have $L_R > 22.7$, clearly above the nominal break between AGNs and starbursts (Miller & Owen 2002). In figure 10 we show a similar plot for the cluster members without radio emission from Miller et al. (2004). Clearly, the distribution of all the galaxies is centered about 1 Mpc southwest of the nominal cluster core, near [15 41 15, 66 16 00] (Owen et al. 1999) and are distributed over a region about 2×6 Mpc in projection. Unlike the impression of two concentrations of radio emitters given by the smaller sample in Owen et al. (1999), the lower luminosity radio emitters are distributed almost uniformly over this large region, and appear even somewhat less clustered than the non-radio emitters. This pattern suggests a fairly uniform distribution of radio-emitting galaxies over the entire projected volume, perhaps avoiding the core of this region. The nominal core of A2125 (where the greatest projected local density of galaxies is found) is not centered in the overall galaxy distribution, and the radio-emitting, star-forming population seems not to be aware of this dense concentration of galaxies. This situation is qualitatively similar to the Cygnus A cluster in which the dense core containing the radio galaxy is offset from the centroid of the overall galaxy distribution (Owen et al. 1997). We find absolutely no correlation between distance from the nominal cluster core and redshift for the radio population. The radio galaxies appear to have radial velocities centered on the cluster mean but including the full range seen in Miller et al.(2003). Thus there is no simple signature of an infalling radio population

In figure 11, we show the cluster members with the same color coding as in figure 9 and figure 10 overlaid on the the *Chandra* 0.5-2.0 keV image (as convolved with a 15 arcsec circular Gaussian). The non-radio detected galaxies do follow the the X-ray distribution in the cluster core and to some extent the more diffuse emission to the southwest. However, the low-luminosity radio emitters (mostly star-forming galaxies) do not show much correlation with the X-ray detections except on the largest scales.

Another perspective on Abell 2125 can seen in figure 12, the HST F814W image of one of the fields in a brighter part of the SW X-ray concentration. Rather than a random distribution of galaxies we find what appear to be several groups of a various sizes. A simple 2D substructure test, not taking into account the magnitudes of the galaxies, shows substructure at $> 96\%$ significance level (Ledlow et al 2000). Thus in this part of the cluster, we seem to be looking through a system made up not of a monolithic cluster but rather many small groups seen in projection.

All of these results plus the broad distribution of radio galaxies in figure 9 suggest that we are dealing with a complex interaction between at least two merging subsystems and that much of the activity appears to be taking place on the outskirts of the two systems, perhaps in group-like environments. The nominal cluster core does not appear to be at the "center" of the large scale cluster but is only one over-dense region in a much larger, complex system. The X-ray luminosity and temperature are also much more consistent with this picture than for a single, monolithic cluster.

4. Discussion

4.1. General Picture of Abell 2125

From our optical and X-ray observations of Abell 2125 we conclude that the vast majority of the radio emitting galaxies in the cluster reflect star formation. The SFRs implied by this emission are relatively modest, $1 - 10$ M$_{\odot}$yr^{-1}. Only a handful of the radio emitters are compact X-ray AGN, about 10%. Most of these are close to our *Chandra* detection limit. Surprisingly, at least 12 more radio objects in the *Chandra* field are not detected by *Chandra* but appear to be AGN, based on a SFI < 1. Several of these are quite clearly FR I or FR II radio galaxies (Dwarakanath & Owen 1999). Essentially all galaxies which are at least 30% brighter than L_* appear to be AGN driven, along with a much smaller percentage of the lower optical-luminosity galaxies. Our 80 ksec *Chandra* exposure does not seem to be deep enough to detect most radio AGN at $z = 0.25$ found in our VLA radio survey of about the same total duration.

Except for four sources in the cluster core, which we will discuss in another paper, both the AGN and the star-forming objects are distributed on a scale of several Mpc and are less clustered than the spectroscopically confirmed non-radio members. Thus the increase in activity we are seeing in Abell 2125 with respect to other rich clusters seems to be taking place on scales closer to a supercluster than a typical cluster core.

From figure 9, we see that the distribution of lower radio luminosity detections is offset from the nominal cluster center about about 1 Mpc and distributed rather uniformly over a region 2×6 Mpc in projection, much like the X-ray emission. In figure 10, we show the locations of the known cluster members without radio detections. One can see that these galaxies appear more clustered than the radio population. Thus the projected distribution suggests that the low luminosity radio population is less clustered than the radio-quiet population and thus is likely to be located in lower density regions in the cluster complex.

From Miller et al. (2004), we see that the entire system can be modeled as an ongoing cluster-cluster merger seen at an angle to the line-of-sight of about 30 degrees. In this picture, the excess star formation is taking place on the scale of the merger, not in the cluster core. Since the major axis of the merging system is near our line-of-sight, the lower density outlying regions of the cluster are projected closer to cluster center than for a more random orientation. This makes the cluster appear richer and accounts for the low X-ray luminosity for such an apparently rich cluster (Miller et al. 2004). In fact, clusters near the upper end of Abell richness must tend to be the ones with their major axis in our line-of-site, since more of the galaxies will be projected into the 2D circle on the sky where richness is estimated. Since the outer parts of clusters are bluer than the cores, such clusters should tend to have larger blue fractions than average, since more of the outer population are projected on the cluster core where the Butcher-Oemler effect is measured (Butcher & Oemler 1984). Thus projection effects explain some of the properties of Abell 2125.

Examination of the outer parts of the cluster with HST (figure 12) shows that many of the galaxies appear to be in small groups. This is an environment one might expect to find on the outskirts of an Abell cluster, in the moderate-density regions of a supercluster. Such environments are more favorable to galaxy interactions and mergers than in regions near the dense core of a cluster. Thus the broad distribution of excess star-forming radio galaxies is consistent with most of the activity we see taking place in such medium density, group environments.

The important question is whether projection effects explain the entire radio excess in Abell 2125 relative to other similar clusters. From Morrison & Owen (2003), the median radio fraction for clusters of similar richness and redshift, considering detected cluster members within 2.5 Mpc of the cluster center, is about 2%. For Abell 2125, the radio fraction is 9%. For clusters similar to Abell 2125 in redshift and richness, only $\sim 20\%$ of the brighter galaxies used in the counts out to 2 Mpc lie within 0.5 Mpc of the cluster core. Thus the richness and radio fraction estimate both describe primarily the properties of galaxies far from the cluster core.

The well-known morphology-density relation (Dressler 1980) shows that at the densities found in rich cluster cores, very few late type galaxies are found and those show evidence for suppressed star formation (Hashimoto et al 1998). However, outside the cluster core at distances ~ 1 Mpc from the cluster center, the fraction of late type galaxies typically rises to $\sim 40\%$, increasing only slowly beyond that distance (Whitmore & Gilmore 1991). Furthermore, Hashimoto et al (1998) suggest that star formation is most active in such intermediate density regions, where galaxy interactions should be most common.

It is likely we are seeing Abell 2125 in some sort of projection. However, as long as most of the observed cluster members are in intermediate density regions, we would expect only a small bias to higher SFR systems with respect to clusters whose major axis is nearer the plane of the sky. However, the excess radio galaxy fraction is four to five times higher than we typically see in other similar rich clusters. In order to explain the high radio fraction in Abell 2125 some other effect must be important. Such an effect could well be that we see Abell 2125 at a special time. Miller et al. (2004) argue that the dynamics of Abell 2125 are consistent with such a picture. Their KMM substructure analysis of the positions and radial velocities of 224 galaxies associated with the cluster find that the Abell 2125 is most consistent with two (or possibly three) velocity systems seen in projection along the line-of-sight. A comparison of the observed dynamics with the n-body merger simulations of Pinkney et al. (1996) show an excellent match to a cluster-cluster merger seen at a viewing angle of about 30 degrees from the line-of-site and within 0.2 Gyr of core passage. Assuming this physical situation, the mass of the entire system also lies within a reasonable range near 10^{15} $M_{\odot}$. Given this picture, several physical mechanisms could be responsible for most of the increase in activity.

4.2. Mechanisms

Numerous mechanisms have been considered which affect the SFR of galaxies in clusters. Certainly, the rate of galaxy mergers, ISM stripping, galaxy harassment, changes in the external pressure and tidal effects all have the potential to increase or decrease the SFR of a galaxy. Most of the work on these subjects has considered galaxies falling radially into a massive cluster. However, the physical situation we are observing appears to be different, i.e. two massive cluster and their associated lower density outskirts involved in a major merger, probably near the point of core passage. Since we are not aware of such a simulation designed to look for the effects relevant to star-formation we will need to extrapolate a bit using the physical effects which have been discussed in a less extreme context.

In a high velocity cluster-cluster merger like Abell 2125, one would expect galaxy-galaxy mergers to be disfavored, since the probability of a galaxy-galaxy merger is proportional to the inverse fourth power of the local velocity dispersion (Gnedin 2003a). However, the details of group-group mergers in such a system might complicate this argument. Nonetheless, we see no direct evidence that galaxy-galaxy mergers play a major role in Abell 2125.

Fujita & Nagashima (1999) conclude that ram pressure on a galaxy radially infalling into a cluster can increase the SFR by a factor of 2 near the cluster core before the rate decreases due to the stripping of the gas. In a complex cluster-cluster merger, the velocity of galaxies relative to the local medium could be much larger than in the infall case. Thus the total ram pressure could easily rise above the values found in the center of an isolated cluster Furthermore, some of the systems in figure 2 show evidence of non-aligned radio emission which could indicate stripping, lending support to ram pressure as a contributer to the increased SFR.

Galaxy harassment (Moore, Lake & Katz 1998), involves the cumulative effects of fast encounters between galaxies in clusters. Most of the impact of this mechanism involves lower-mass galaxies near the cluster core. Since most of the activity we see is far from the core of Abell 2125 and involves relatively massive galaxies, it seem unlikely this mechanism has much to do with the effects we are seeing.

Tidal effects in clusters have been recently considered by a number of papers as a way to affect galaxy morphology and SFRs. Byrd & Valtonen (1990) and Henriksen & Byrd (1996) argue that the tidal effect of the cluster potential on an infalling galaxy would create more star-formation activity than stripping by the IGM. Bekki (1999) studied the case of the tidal effects on a spiral in a group, as the group falls into a more massive cluster; besides driving a transient starburst, the variable tidal field of the group heats the disk and ultimately leads to an S0 morphology. Gnedin (2003a) simulates the general case of galaxies falling into a cluster in the presence of the time varying tidal field resulting from other substructure which also is in the process of falling in. The simulation shows that in the frame of an infalling galaxy there exists a strongly time-variable tidal field with multiple major events far from the cluster core. Gnedin (2003b) concludes that this process leads to the transformation of spirals into S0's.

4.3. Application to Abell 2125

The case we see in Abell 2125 is somewhat different than discussed in the previous section in that we seem to be seeing a major merger close to core passage. Thus the mechanisms discussed above need to be considered at this special time, which is supported by the fact that Abell 2125 stands out from other rich clusters that have been studied at similar redshifts (Morrison & Owen 2003). At a later time one should expect A2125 to have settled down and to have evolved into a rich cluster like those we see locally.

In such a dynamic case, the time-variable tidal effects must be especially extreme. It thus seems likely that the effects described by Bekki (1999) and Gnedin (2003a) must be especially important. However, not enough time will have passed for the systems to reach their ultimate fate. The observations show an excess of galaxies with active star-formation but 37% of these systems have optical concentration indices lying between disks and $r^{1/4}$ laws. They also have SEDs far from young objects one might associate with bursts of recent star-formation.

This pattern seems consistent with star formation related to the strongly time-variable tidal forces as analyzed in Bekki (1999) and Gnedin (2003a). Once the event is over, these galaxies seem on their way to becoming dull S0's as described by Gnedin (2003a). The distribution of concentration indices suggests that many of our detected systems are neither pure disks nor $r^{1/4}$ spheroids. Thus the structures of many of the radio galaxies (see figure 3) are consistent with objects which have experienced tidal heating. However, the analysis of Bekki (1999) and Gnedin (2003b) suggest that the timescale for the transition from disk to S0 is very long, many Gyrs, while the gas-dynamic processes which led to star-formation have much shorter timescales. Thus the broad distribution of concentration indices associated with the radio galaxies either suggests that tidal heating has been taking place for some time or that the tidal forces are larger in the Abell 2125 case leading to more rapid evolution of the stellar distribution. A more targeted analysis of tidal effects during a major cluster-cluster merger is needed to understand better how tidal (and other) effects would affect a system like Abell 2125. But given that cluster-cluster mergers are quite common events, our observational results suggest that core passage during a major cluster-cluster is may be an especially important time in galaxy evolution.

5. Conclusions

The excess levels of radio emission in Abell 2125 are dominantly related to star formation. Abell 2125 is a cluster-cluster merger seen in projection. Active star formation is not associated with the cluster core but spread fairly uniformly throughout a 2×6 Mpc region in projection. This activity must be taking place in intermediate density regions, mostly in groups associated with the outskirts of the merging clusters.

The cluster-cluster merger seen in projection accounts for the relatively low X-ray luminosity and temperature, combined with the very high richness and relatively high Butcher-Oemler blue fraction. The excess radio population also is at least partly explained by projection effects. However, the large radio population seems also to require some other mechanism to explain the four to five times larger radio fraction than is seen in other such clusters. This extra factor may be due to the cluster-cluster merger being seen very close to core passage where the interactions of the two cluster systems should be greatest.

It seems likely that star-formation has been stimulated in the outlying group environments associated with the clusters during the time near the core passage. The variations in the tidal field, experienced by each galaxy due to the changing substructure and its position relative to each galaxy seems to be the most likely origin for the enhanced SFRs seen in Abell 2125. The activity in Abell 2125, combined with its dynamical state close to core passage of a major cluster-cluster merger, suggests that this phase in cluster evolution may be particularly important for galaxy evolution.

The authors thank A. Klypin for useful discussions about the large scale structure and J. Eilek for comments on the text.

REFERENCES

Abraham R.G., Valdes, F, Yee, H.K.C., & Van Den Bergh, S. 1994, ApJ, 432, 75

Bekki, K. 1999, ApJ, 510, L15

Bekki, K., Couch, W. J. & Shioya, Y. 2002, ApJ, 577, 651

Bolzonella, M., Miralles, J.-M., & Pelló, R. 2000, A&A, 363, 476

Bruzual, G. & Charlot, S. 1993, ApJ, 405, 538

Butcher, H. & Oemler, A. 1984, ApJ, 285, 426

Byrd, G. & Valtonen, M. 1990, ApJ, 350, 89

Calzetti, D., Armus, L., Bohlin, R. C., Kinney, A. L., Koornneef, J., & Storchi-Bergmann, T. 2000, ApJ, 533, 682

Colbert, E. J. M., Baum, S. A., Gallimore, J. F., O'Dea, C. P. & Christensen, J. A. 1996, ApJ, 467, 551

Condon, J. J. 1992, A&A Rev., 30, 575

Condon, J. J., Cotton, W. D. & Broderick, J. J. 2002, AJ, 124, 675

Dressler, A., ApJ, 236, 351

Dwarakanath, K. S. & Owen, F. N. 1999, AJ, 118, 625

Fujita, Y. 1999, ApJ, 509, 587

Fujita, Y. & Nagashima, M. 1999, ApJ, 516, 619

Gnedin, O. Y. 2003a, ApJ, 582, 141

Gnedin, O. Y. 2003b, ApJ, 589, 752

Hashimoto, Y., Oemler, A., Lin, H., & Tucker, D. 1998, ApJ, 499, 589

Henriksen, M., & Byrd, G. 1996, ApJ, 459, 82

Ledlow, M. J. & Owen, F. N. 1996, AJ, 112, 9

Ledlow, M. J., Owen, F. N., Keel, W. C. & Andersen, V. 2000, Ap&SS, 269, 613

Miller, N. A. 2001, PhD Thesis, New Mexico State University

Miller, N. A. & Owen, F. N. 2002, AJ, 124, 2453

Miller, N. A., Owen, F. N., Oegerle, W., Keel, W., & Ledlow, M. 2004, ApJ, in press (astro-ph/406292)

Moore, B., Lake, G. & Katz, N. 1998, ApJ, 495, 139

Morrison, G. E. & Owen, F. N. 2003, AJ, 125, 506

Owen, F. N., Ledlow, M. J. & Keel, W. C. 1995, AJ, 109, 14

Owen, F. N., Keel, W. C., Ledlow, M. J., G.E. Morrison & Windhorst, R. A. 2004a, submitted

Owen, F. N., Keel, W. C., Wang, Q. D., & Ledlow, M. J. 2004b, in preparation

Owen, F. N., Ledlow, M. J., Keel, W. C., & Morrison, G. E, 1999, AJ, 118, 633

Owen, F. N., Ledlow, M. J., Morrison, G. E., & Hill, J. M. 1997, ApJ, 488, L15

Pinkney, J., Roettiger, K., Burns, J. O., & Bird, C. M. 1996, ApJS, 104, 1

Ranalli, P., Comastri, A., & Setti, G. 2003, A&A, 399, 39

Wang, Q. D. 2004 ApJ, in press (astro-ph/0405272)

Wang, Q. D., Connolly, A. & Brunner, R. J. 1997, ApJ, 487, L13

Wang, Q. D., Owen, F. N., & Ledlow, M. J. 2004, ApJ, in press (astro-ph/0404602)

Whitmore, B. C. & Gilmore, D. M. 1991, ApJ, 367, 64

Yun, M. S., Reddy, N. A., & Condon, J. J. 2001, ApJ, 554, 803

Williams, R. E., Blacker, B., Dickinson, M., Dixon, W. V., Ferguson, H. C., Fruchter, A. S., Giavalisco, M., Gilliland, R. L., Heyer, I., Katsanis, R., Levy, Z., Lucas, R. A., McElroy, D. B., Petro, L., Postman, M., Adorf, H., & Hook, R. N. AJ, 112, 1335

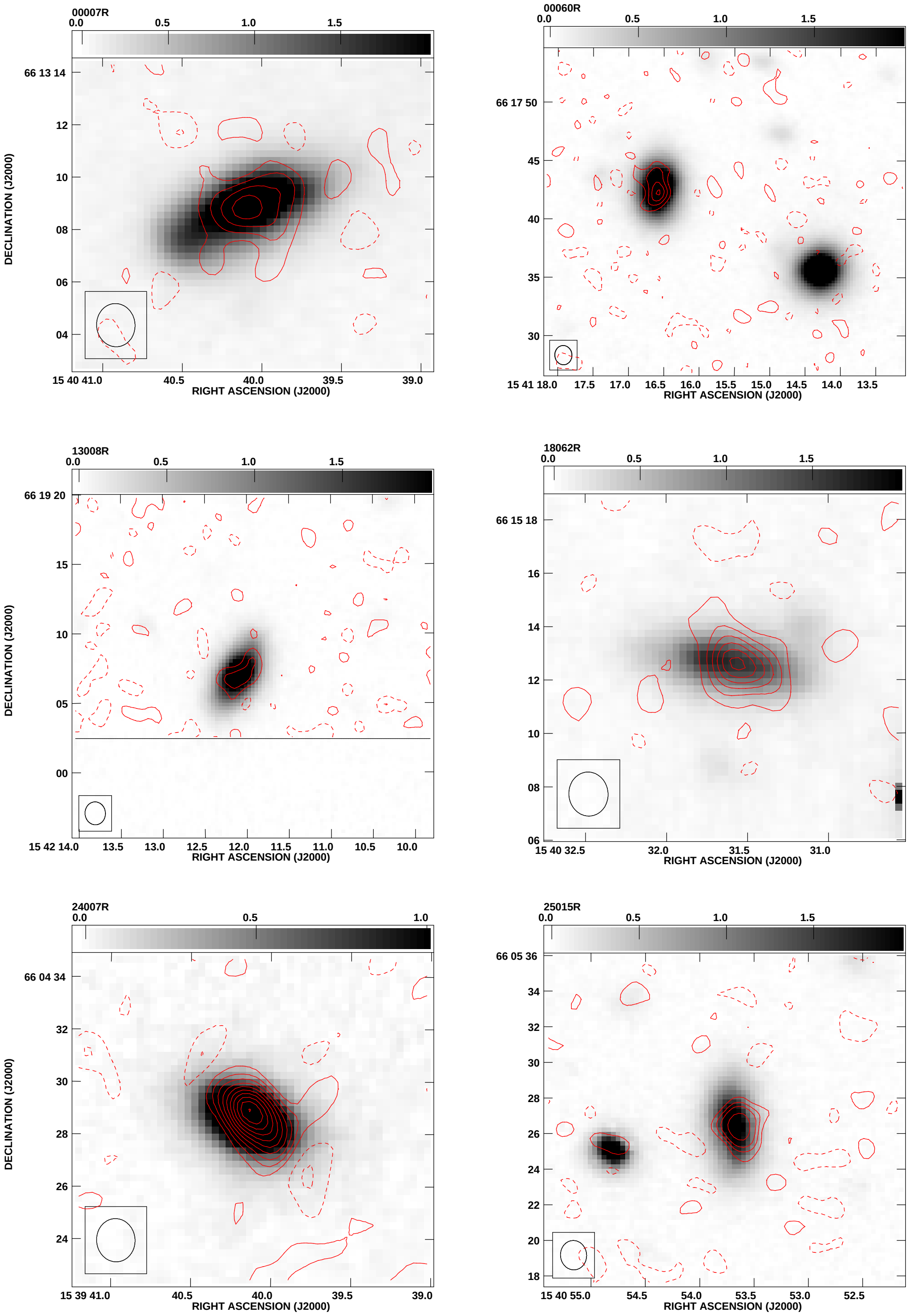

Fig. 1.— Examples of Radio Galaxies with Aligned Radio/Optical Emission.

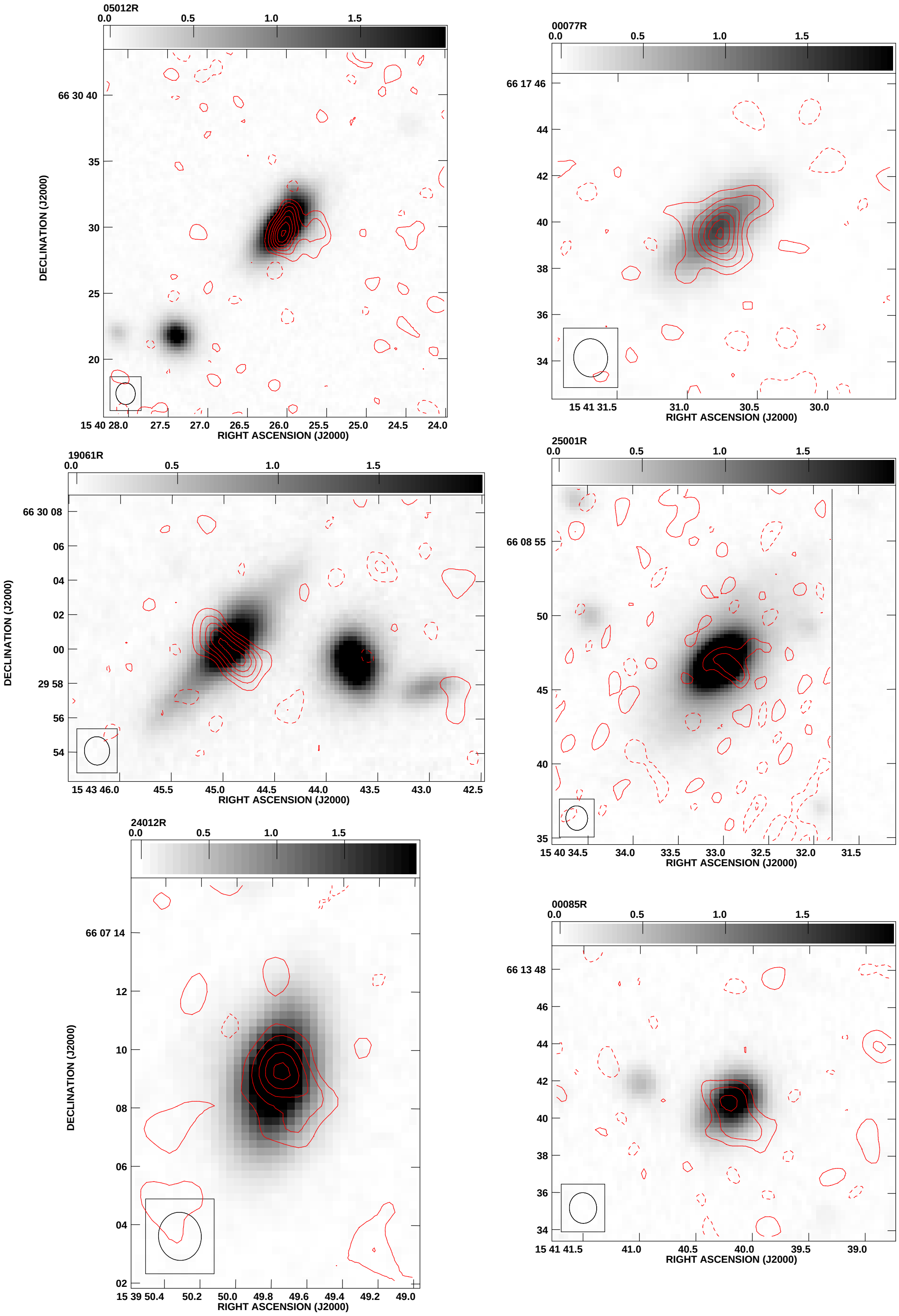

Fig. 2.— Examples of Radio Galaxies with Some Misaligned Radio/Optical Emission.

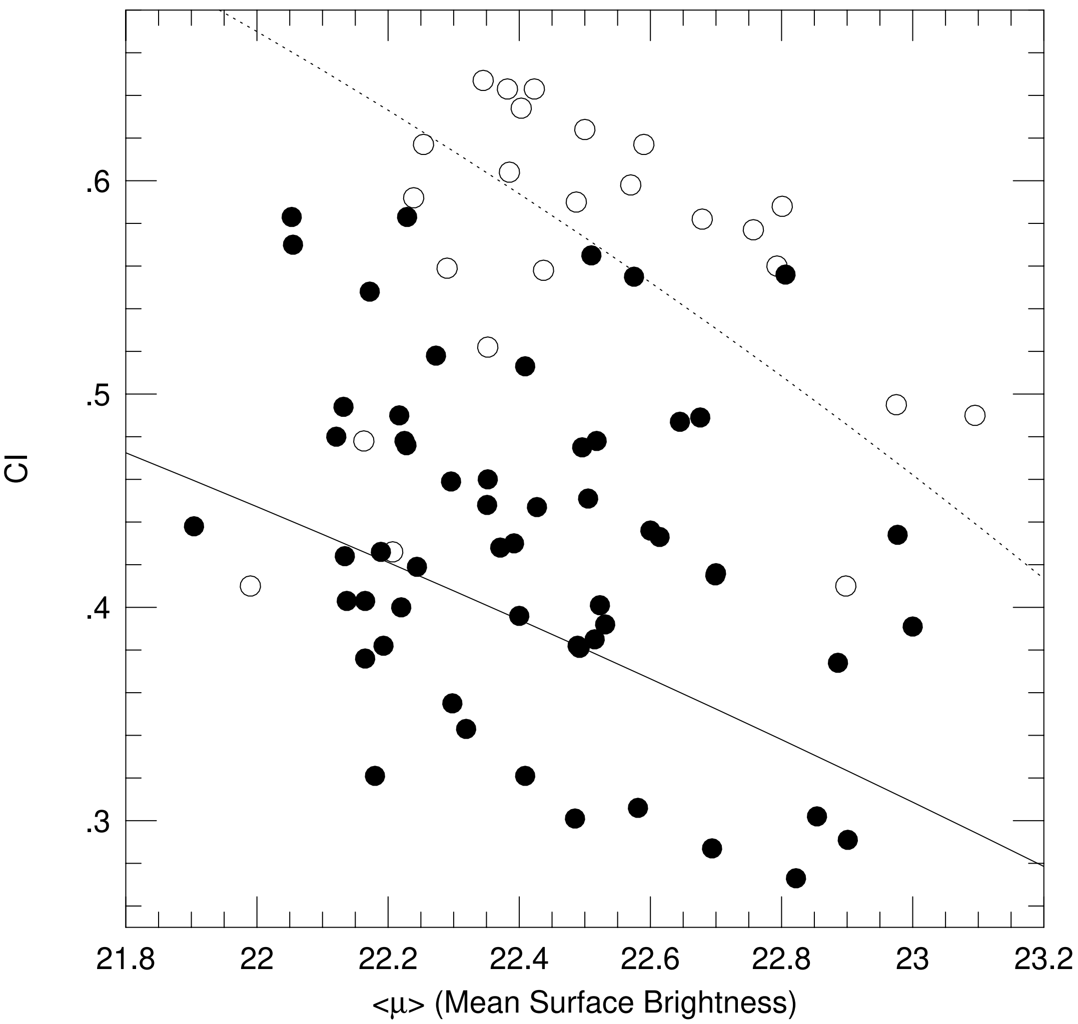

Fig. 3.— Concentration Index for the radio detected galaxies in A2125 plotted versus Mean Surface Brightness. The theoretical curves for $r^{1/4}$ laws (dotted line) and exponential disks (solid line) are also plotted. The solid symbols are galaxies which has a Star Formation Index, $SFI > 1$, indicating some evidence of active star-formation. The open circles have $SFI \leq 1$ indicating little or no evidence for star-formation activity.

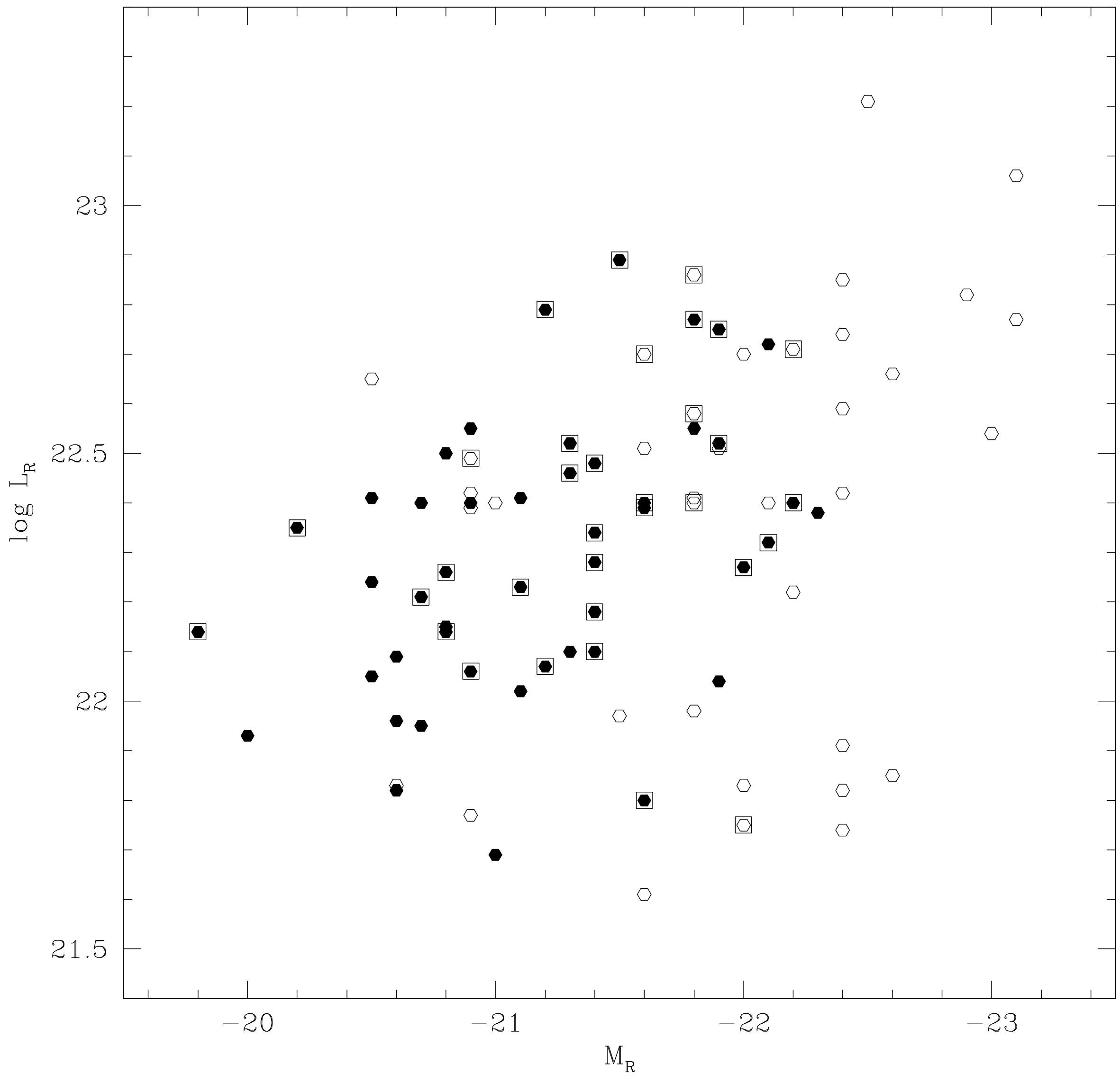

Fig. 4.— R absolute magnitude versus log of the 20cm absolute radio luminosity (W/Hz). Solid symbols indicate sources with line emission. Boxes indicate objects for which the radio emission is aligned with the optical major axis.

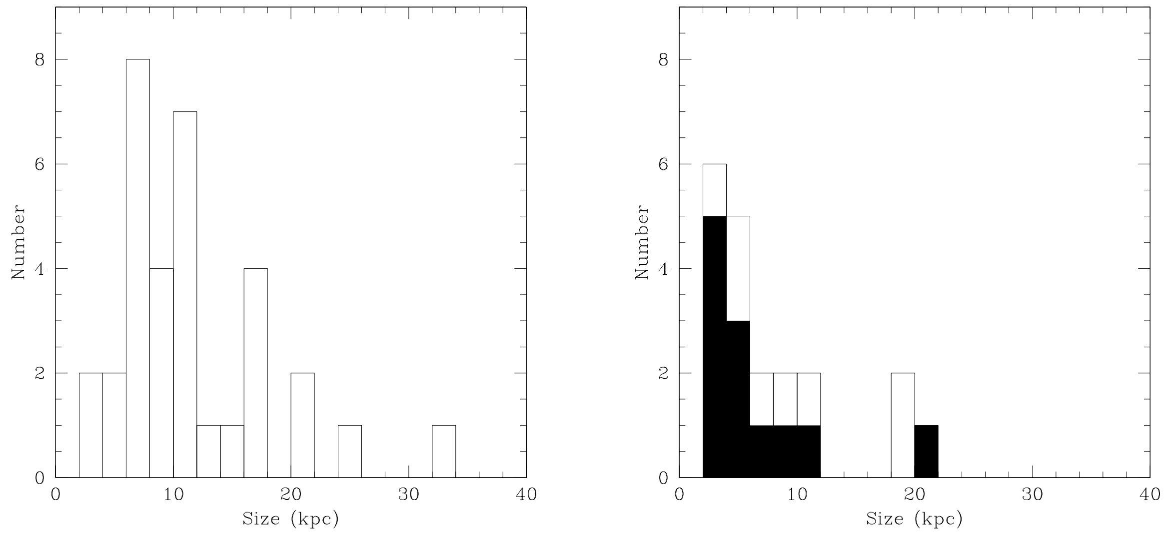

Fig. 5.— Radio linear size histograms. The left panel contains all radio/optical aligned sources. The right panel includes only non-aligned sources with emission lines. The solid boxes represent sources with upper limits to their radio sizes.

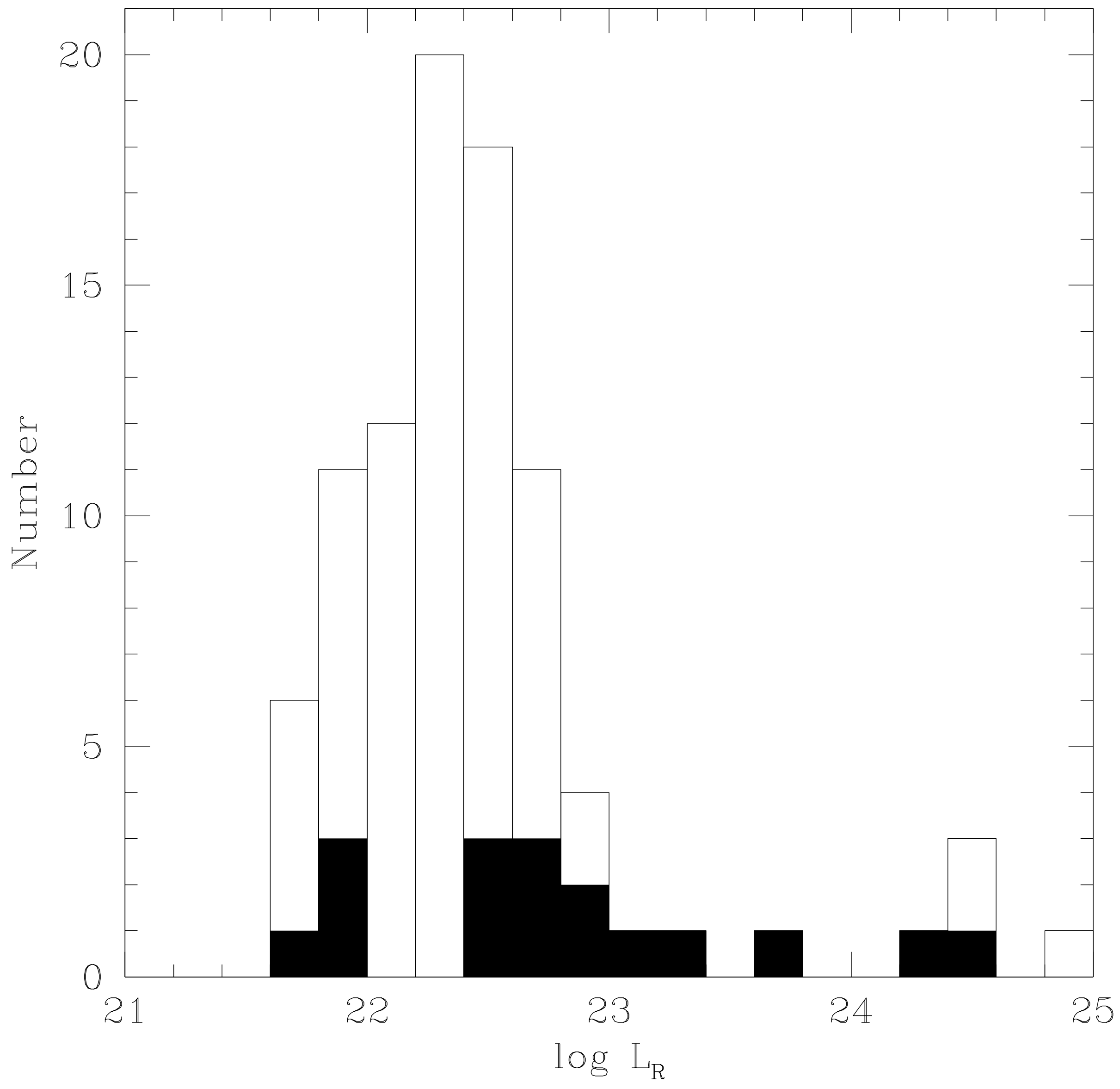

Fig. 6.— Histogram of log of the 20cm absolute radio luminosity. Solid boxes indicate objects for which the optical absolute magnitude is brighter than −22.3.

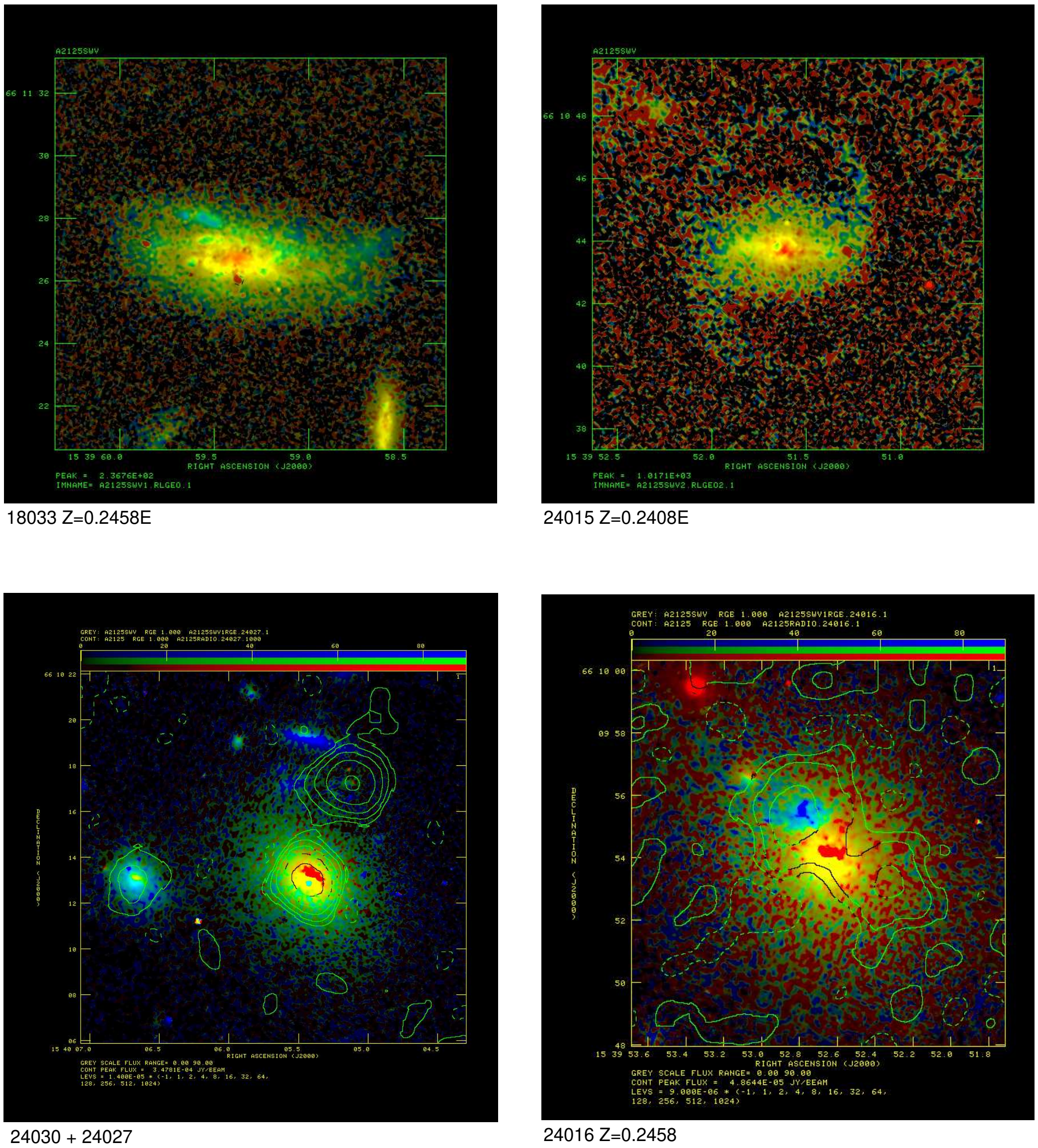

Fig. 7.— Examples of the Diverse Structures seen HST Images of Radio Galaxies. The radio contours are overlaid in the lower two panels. Comments on each image are given in the text.

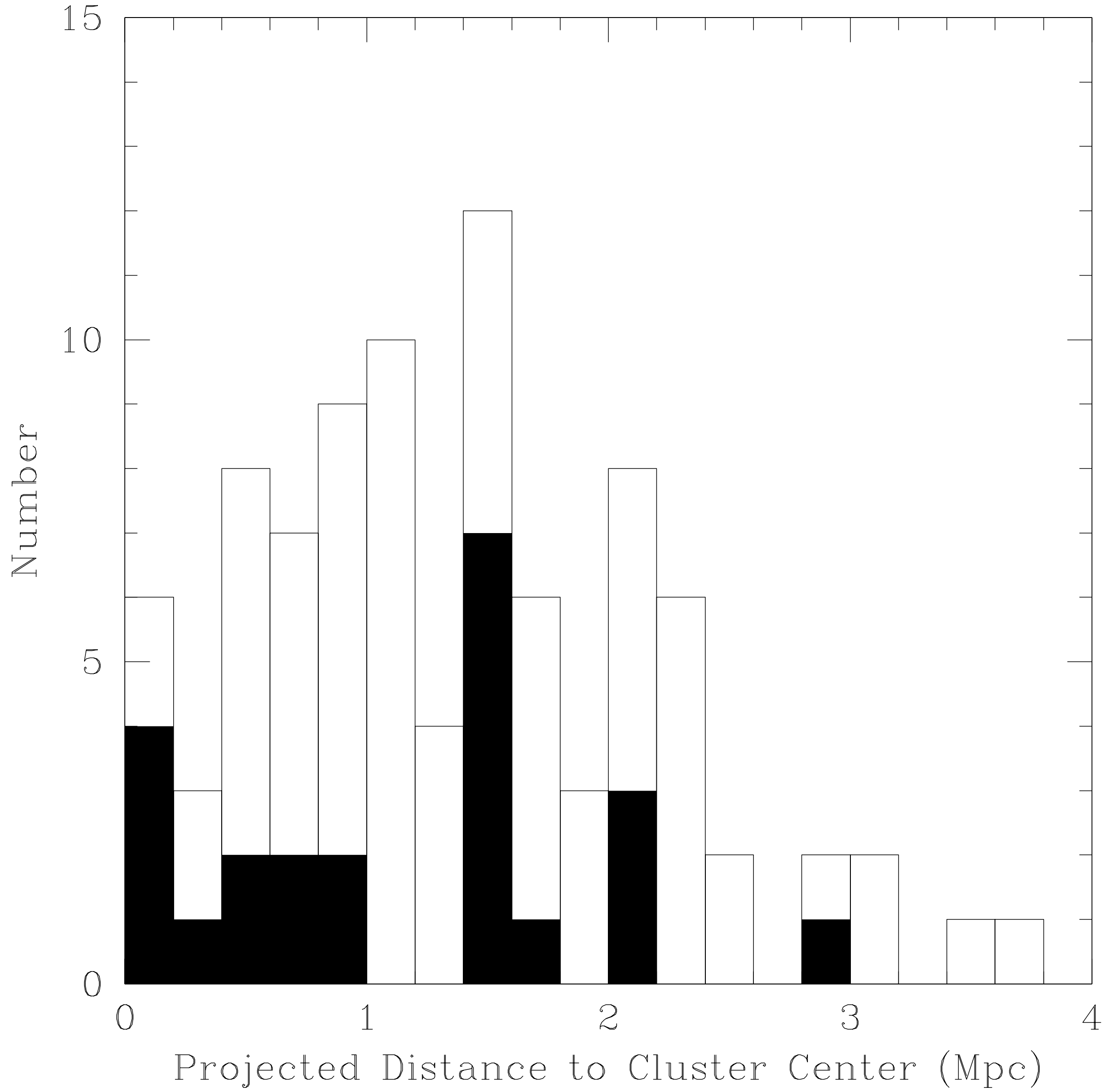

Fig. 8.— Histogram of the distance of radio detected galaxies from the cluster center in Mpc. The solid boxes indicate objects, with $SFI < 1$, the most likely AGN.

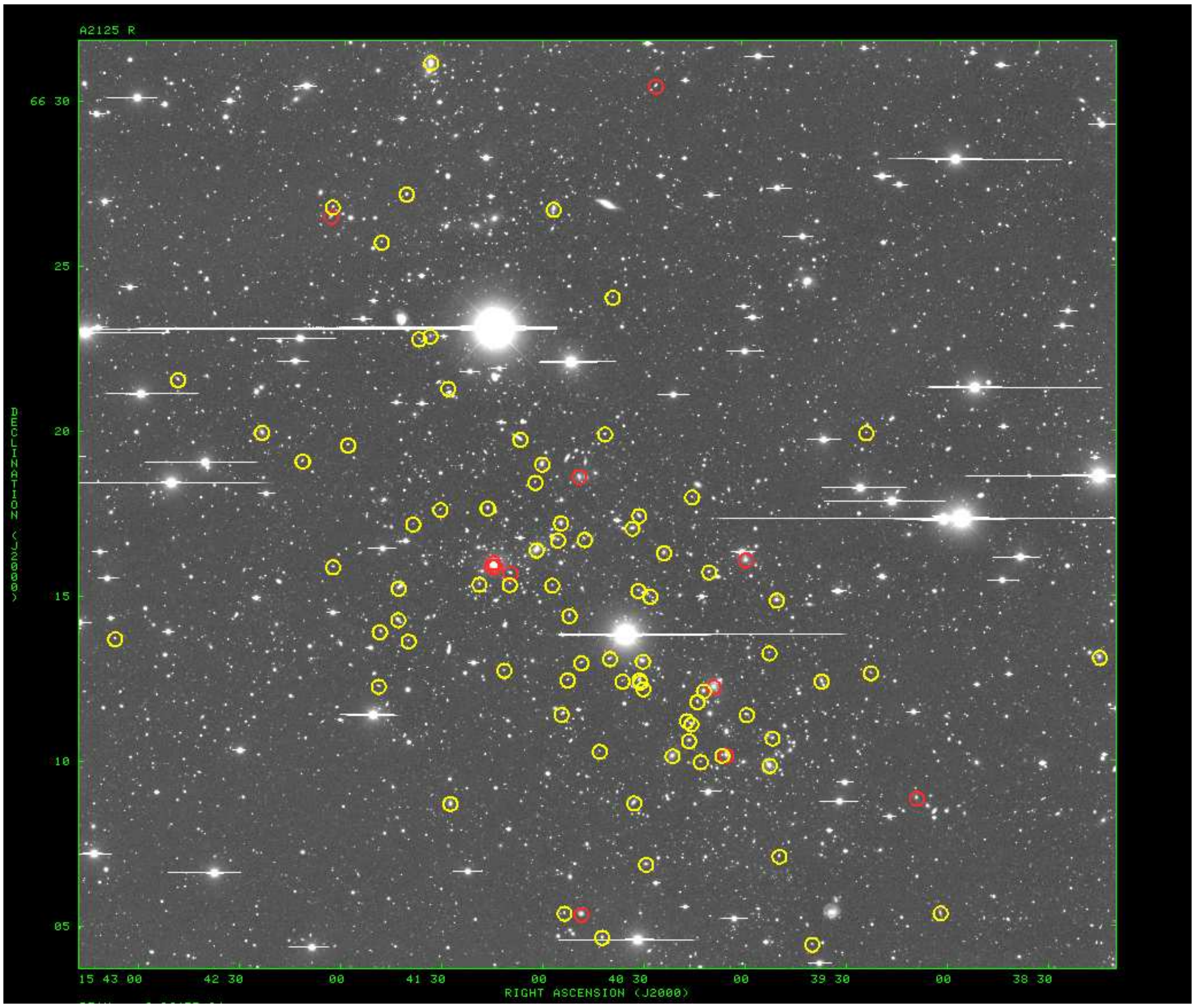

Fig. 9.— Spectroscopically confirmed members with radio detections overlayed on the optical R image. Red circles are for radio sources with log $L_R > 22.7$. Yellow circles are for $L_R \leq 22.7$ The nominal cluster center is at (15 41 14, 66 15 00); see figure 11. The field is about 6.3 Mpc on a side in projection at Abell 2125.

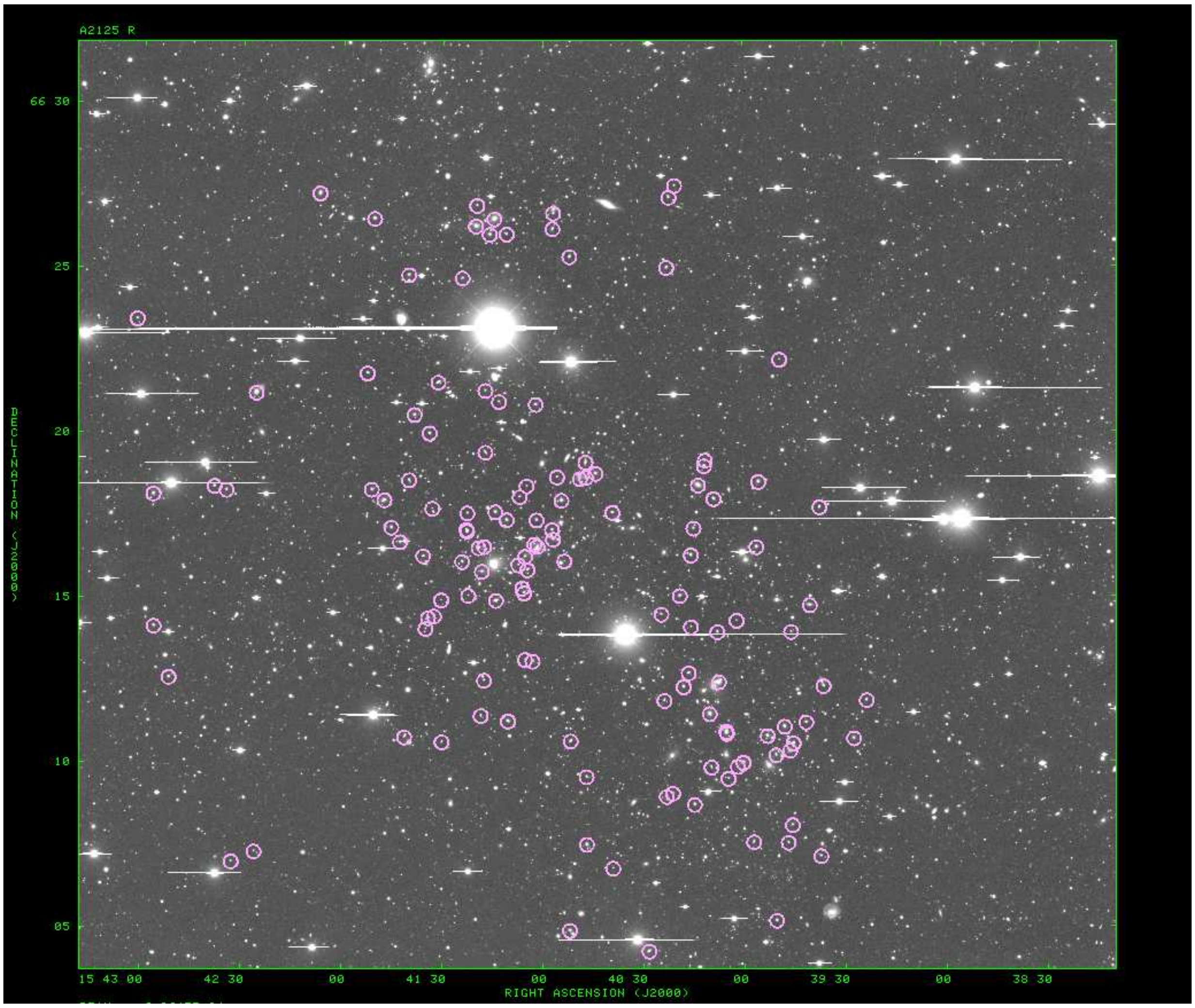

Fig. 10.— Spectroscopically confirmed members without radio emission overlayed on the R optical image.

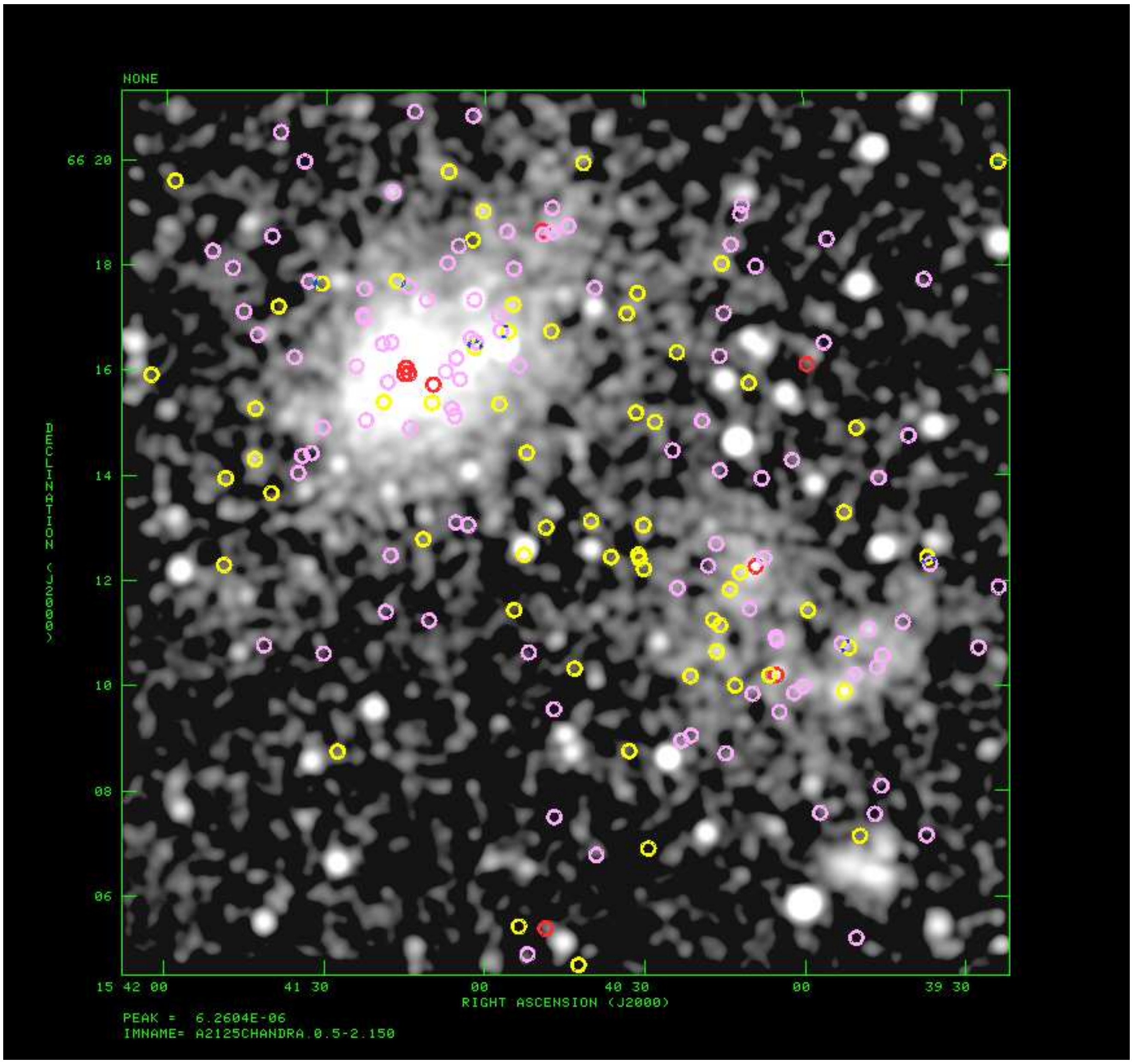

Fig. 11.— Cluster Members overlaid on the the 0.5-2.0 keV *Chandra* image of Abell 2125 convolved with a 15 arcsec Gaussian. The same color coding is used as in figures 9 and 10

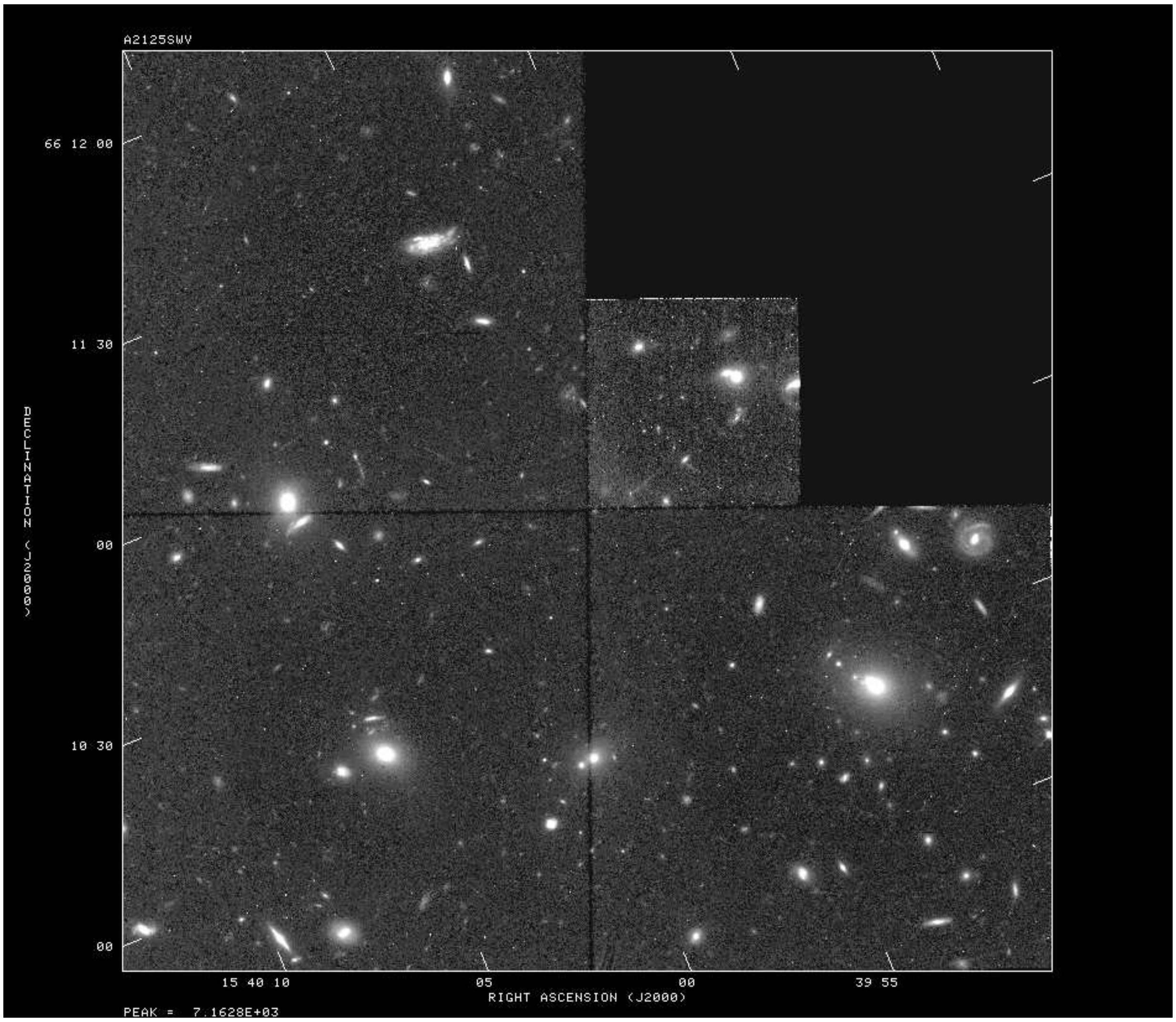

Fig. 12.— HST WFPC2 Image of a region in the SW extension of A2125 about 1.8 Mpc southwest of the nominal cluster center in projection. The image is about 500 kpc on a side in projection. Note the non-random distribution of galaxies consistent with looking through a number of small groups instead of a random cluster field.

Table 1. A2125 Member Radio Sources

Name	RA(2000.0)	Dec(2000.0)	Dist Mpc	Peak μJy/b	Total μJy	Size arcsec	z
17017	15 38 13.80(0.08)	66 13 05.9(0.5)	18.3	32.1	148.5(33.)	<2.2	0.2475
23009	15 39 01.94(0.09)	66 05 24.2(0.5)	16.5	39.8	300.6(85.)	4.1	0.2575
23016	15 39 08.69(0.02)	66 08 52.8(0.1)	14.1	764.1	60235.0(1829.)	25.0	0.2449
18013	15 39 22.18(0.05)	66 12 41.6(0.3)	11.5	75.1	152.4(15.)	<1.3	0.2449e
11700	15 39 23.16(0.09)	66 19 57.7(0.5)	12.2	25.3	53.3(15.)	<2.5	0.2442e
18023	15 39 36.86(0.04)	66 12 27.0(0.3)	10.1	109.1	191.6(14.)	<1.2	0.2448
24007	15 39 40.10(0.05)	66 04 28.7(0.3)	14.2	128.5	364.1(26.)	1.0x0p=46	0.2468e
24012	15 39 49.73(0.06)	66 07 99.1(0.4)	11.6	62.2	170.8(26.)	1.6x0.5p=5	0.2445e
18700	15 39 50.14(0.08)	66 14 54.7(0.5)	8.4	27.1	39.7(10.)	<1.8	0.2458
24015	15 39 51.62(0.08)	66 10 43.8(0.5)	9.3	42.6	114.7(29.)	2.6x0p=108	0.2408e
18030	15 39 52.47(0.06)	66 13 18.5(0.4)	8.4	55.6	83.3(11.)	<0.9	0.2482e
24016	15 39 52.52(0.07)	66 09 54.3(0.4)	9.7	50.6	270.1(48.)	3.6	0.2458
18033	15 39 59.31(0.04)	66 11 26.6(0.3)	8.3	166.4	348.4(23.)	2.0x0.7p=71	0.2458e
18072	15 39 59.43(0.02)	66 16 07.5(0.1)	7.6	600.4	10668.0(335.)	99.0	0.2459
24027	15 40 05.34(0.03)	66 10 12.9(0.2)	8.4	359.5	970.0(45.)	4.6	0.2425
24030	15 40 06.60(0.08)	66 10 12.8(0.5)	8.3	38.3	82.6(21.)	1.9x0p=156	0.2436e
18041	15 40 09.11(0.05)	66 12 17.1(0.3)	7.1	114.3	390.0(30.)	2.3x0.6p=75	0.2455
18701	15 40 10.34(0.09)	66 15 46.2(0.6)	6.5	32.3	149.1(46.)	8.5x2.0p=156	0.2477
18042	15 40 12.05(0.03)	66 12 09.9(0.2)	6.9	167.5	330.5(15.)	<0.7	0.2558
24111	15 40 13.05(0.10)	66 10 01.1(0.6)	7.9	27.3	107.2(42.)	5.5x0p=93	0.2460e
18045	15 40 13.98(0.09)	66 11 50.7(0.5)	6.8	35.1	62.1(17.)	1.6x0p=71	0.2458e
18047	15 40 15.38(0.08)	66 18 02.5(0.5)	6.6	43.6	101.2(22.)	2.2x0.6p=54	0.2433e
18048	15 40 15.84(0.04)	66 11 09.9(0.3)	7.0	134.6	334.3(23.)	1.7x1.5p=57	0.2455e
24701	15 40 16.49(0.08)	66 10 39.7(0.5)	7.2	29.8	39.9(9.)	<1.9	0.2559
18702	15 40 17.14(0.12)	66 11 15.9(0.7)	6.8	25.8	37.6(19.)	2.7x0p=115	0.2443e
24033	15 40 21.42(0.07)	66 10 12.1(0.4)	7.2	36.6	48.8(9.)	<1.9	0.2565
18703	15 40 23.87(0.12)	66 16 21.4(0.7)	5.2	21.8	33.5(18.)	2.5x0p=84	0.2500
05012	15 40 26.03(0.06)	66 30 29.5(0.3)	16.2	88.9	426.7(49.)	1.8x0.8p155	0.2573
18070	15 40 28.02(0.09)	66 15 01.9(0.5)	4.6	29.8	50.3(15.)	1.5x0.6p=80	0.2475e
24115	15 40 29.36(0.07)	66 06 55.1(0.4)	9.3	35.6	56.6(11.)	<1.3	0.2421

Table 1—Continued

Name	RA(2000.0)	Dec(2000.0)	Dist Mpc	Peak μJy/b	Total μJy	Size arcsec	z
18056	15 40 30.13(0.04)	66 12 14.2(0.3)	5.2	144.3	195.0(12.)	0.9x0p=123	0.2456e
18057	15 40 30.23(0.05)	66 13 04.1(0.3)	4.8	114.7	151.2(12.)	1.20x0p=27	0.2494e
18300	15 40 30.98(0.09)	66 12 26.2(0.5)	5.0	25.3	29.2(8.)	<2.0	0.2458e
18060	15 40 31.21(0.06)	66 12 30.5(0.3)	5.0	81.2	199.2(24.)	2.6x1.5p=3	0.2474e
18061	15 40 31.27(0.08)	66 17 28.9(0.5)	5.0	43.9	98.2(24.)	3.1x1.9p=4	0.2430
18062	15 40 31.55(0.06)	66 15 12.6(0.3)	4.3	76.1	149.3(18.)	1.9x0.8p=66	0.2444e
25001	15 40 32.93(0.09)	66 08 46.7(0.5)	7.5	35.6	143.4(41.)	4.9x2.5p=68	0.2430e
00002	15 40 33.28(0.04)	66 17 05.8(0.2)	4.6	137.4	156.7(9.)	<0.9	0.2548
00600	15 40 36.31(0.07)	66 12 28.0(0.4)	4.6	35.0	39.4(8.)	<1.5	0.2423e
12004	15 40 39.09(0.09)	66 24 05.8(0.5)	9.7	40.0	67.9(19.)	1.7x0p=15	0.2381e
00007	15 40 40.05(0.07)	66 13 08.9(0.4)	3.9	56.3	150.4(24.)	2.7x1.1p=104	0.2462e
12007	15 40 41.44(0.09)	66 19 57.2(0.6)	5.9	39.0	74.8(23.)	3.1x0p=137	0.2429e
25100	15 40 42.46(0.09)	66 04 42.5(0.5)	10.8	34.9	210.1(57.)	4.8x2.3p=107	0.2521e
25010	15 40 43.17(0.03)	66 10 20.6(0.2)	5.6	222.0	264.7(12.)	<0.7	0.2558
00700	15 40 47.55(0.10)	66 16 45.5(0.6)	3.2	24.8	40.6(16.)	2.1x0p=47	0.2469
00014	15 40 48.54(0.08)	66 13 01.3(0.5)	3.2	34.5	182.2(42.)	5.5x4.7p=127	0.2423
25702	15 40 48.63(0.06)	66 05 24.1(0.4)	9.9	79.6	419.8(52.)	11.03x6.5p=14	0.2561
00104	15 40 49.16(0.02)	66 18 39.8(0.1)	4.4	504.0	16108.0(497.)	25.0	0.2433
00020	15 40 52.14(0.08)	66 14 27.0(0.5)	2.3	32.1	144.6(37.)	4.5x1.7p=9	0.2419e
00022	15 40 52.63(0.05)	66 12 30.4(0.3)	3.3	97.2	190.5(16.)	1.5x1.3p=96	0.2588e
25015	15 40 53.63(0.05)	66 05 26.4(0.3)	9.8	94.3	153.5(12.)	<1.0	0.2508e
00026	15 40 54.49(0.04)	66 11 27.4(0.2)	4.1	191.3	210.0(10.)	<0.7	0.2484e
00027	15 40 54.67(0.03)	66 17 15.7(0.2)	3.0	246.0	310.1(13.)	0.8x0.5p=119	0.2560e
00028	15 40 55.56(0.06)	66 16 44.7(0.4)	2.5	53.3	55.5(7.)	<1.1	0.2486
12027	15 40 56.88(0.06)	66 26 45.6(0.3)	11.9	122.5	308.6(35.)	3.1x0.6p=167	0.2463
00031	15 40 57.30(0.08)	66 15 22.5(0.5)	1.7	51.6	96.0(19.)	2.7x0p=16	0.2545e
00034	15 41 00.33(0.07)	66 19 02.5(0.4)	4.3	37.8	41.9(8.)	<1.0	0.2395
00039	15 41 01.93(0.03)	66 16 26.6(0.2)	1.9	202.7	207.2(9.)	<0.8	0.2457
00201	15 41 02.33(0.06)	66 18 29.4(0.4)	3.7	38.7	72.7(10.)	<5.4	0.2454e
12033	15 41 06.84(0.09)	66 19 47.5(0.5)	4.8	32.0	125.0(35.)	4.2x1.7p=55	0.2406e

Table 1—Continued

Name	RA(2000.0)	Dec(2000.0)	Dist Mpc	Peak μJy/b	Total μJy	Size arcsec	z
00047	15 41 09.73(0.02)	66 15 44.5(0.1)	0.9	21783.0	22944.0(689.)	14.0	0.2528e
00703	15 41 09.97(0.08)	66 15 23.6(0.5)	0.6	35.6	156.2(38.)	6.3x4.7p=55	0.2494
00051	15 41 11.59(0.09)	66 12 47.9(0.6)	2.2	33.0	54.4(18.)	2.5x0p=113	0.2473e
00057	15 41 14.37(0.02)	66 15 57.1(0.1)	1.0	1300.0	2910.0(90.)	2.8x0.8p=12	0.2518
00105	15 41 14.87(0.04)	66 16 03.8(0.2)	1.1	272.0	677.0(33.)	4.0	0.2470
00106	15 41 15.24(0.02)	66 15 56.7(0.1)	1.0	1052.0	15712.0(477.)	23.0	0.2466
00060	15 41 16.60(0.08)	66 17 42.6(0.5)	2.7	47.4	112.1(23.)	2.9x0.8p=178	0.2422e
00701	15 41 19.06(0.09)	66 15 24.2(0.5)	0.6	24.2	24.2(7.)	<2.3	0.2480
25701	15 41 27.59(0.09)	66 8 45.6(0.5)	6.4	25.6	32.5(9.)	<1.3	0.2454
12068	15 41 28.51(0.06)	66 21 20.1(0.4)	6.5	53.4	67.1(9.)	<1.4	0.2484e
00077	15 41 30.76(0.06)	66 17 39.5(0.3)	3.1	76.5	132.4(15.)	1.6x0.9p=163	0.2516e
06008	15 41 33.87(0.05)	66 31 11.7(0.3)	16.3	96.4	347.1(27.)	<1.2	0.2369
12058	15 41 33.89(0.05)	66 22 54.7(0.3)	8.2	105.5	149.6(11.)	<0.9	0.2514
12100	15 41 37.29(0.09)	66 22 49.8(0.5)	8.2	36.6	104.4(29.)	2.9x0p=104	0.2488e
00084	15 41 38.90(0.06)	66 17 13.3(0.4)	3.3	62.6	82.7(11.)	1.2x0.2p=24	0.2397e
00085	15 41 40.16(0.08)	66 13 40.3(0.5)	3.0	41.0	145.8(31.)	3.7x1.4p=37	0.2517
12702	15 41 41.13(0.08)	66 27 12.7(0.5)	12.5	29.3	65.3(16.)	<3.1	0.2398e
00089	15 41 43.23(0.05)	66 15 16.6(0.3)	3.0	128.8	152.1(12.)	1.4x0.4p=145	0.2518
00704	15 41 43.28(0.06)	66 14 19.2(0.3)	3.0	97.2	297.8(34.)	8.1x6.1p=179	0.2547
12061	15 41 48.61(0.05)	66 25 45.4(0.3)	11.3	80.0	151.1(14.)	<0.9	0.2492e
00705	15 41 48.77(0.07)	66 13 57.2(0.4)	3.7	62.8	193.8(34.)	9.3x5.0p=129	0.2444
00098	15 41 49.03(0.06)	66 12 18.2(0.3)	4.4	66.1	74.6(8.)	<0.9	0.2473e
13700	15 41 58.49(0.08)	66 19 36.4(0.5)	6.4	27.7	35.0(9.)	<1.4	0.2534
19011	15 42 02.85(0.10)	66 15 54.8(0.6)	5.0	38.2	69.4(25.)	4.6x0p=101	0.2412e
13003	15 42 03.39(0.08)	66 26 48.7(0.5)	12.8	45.3	179.4(43.)	2.8x0p=101	0.2468e
13004	15 42 03.82(0.06)	66 26 31.8(0.4)	12.6	80.4	458.6(60.)	4.3x0p=151	0.2458e
13008	15 42 12.07(0.09)	66 19 07.0(0.6)	7.1	34.0	89.5(28.)	3.2x0p=121	0.2501e
13015	15 42 24.27(0.05)	66 19 58.3(0.3)	8.6	141.7	231.2(17.)	1.3x0p=127	0.2473
13702	15 42 49.60(0.07)	66 21 33.2(0.4)	11.6	71.5	224.4(40.)	6.6x4.1p=175	0.2390
19061	15 43 07.80(0.08)	66 13 41.4(0.5)	11.5	46.5	129.0(29.)	2.0x0p=72	0.2394e

Table 1—Continued

Name	RA(2000.0)	Dec(2000.0)	Dist Mpc	Peak μJy/b	Total μJy	Size arcsec	z

Table 2. Templates

Spec Type	Number	SFR	Timescale
Burst	1	Single Burst	—
E	2	Exponential	$\tau = 1$ Gyr
S0	3	Exponential	$\tau = 2$ Gyr
Sa	4	Exponential	$\tau = 3$ Gyr
Sb	5	Exponential	$\tau = 5$ Gyr
Sc	6	Exponential	$\tau = 15$ Gyr
Sd	7	Exponential	$\tau = 30$ Gyr
Im	8	Constant	—

Table 3. A2125 Gunn-Oke Magnitudes

Name	U	B	V	R	I	8010	9170	J	H	K
17017	22.08	20.65	19.36	18.45	17.93	17.94	17.50	−9.00	−9.00	−9.00
23009	22.71	21.38	20.08	19.10	18.47	18.44	18.05	−9.00	−9.00	−9.00
23016	22.30	21.00	19.74	18.84	18.39	18.35	17.99	−9.00	−9.00	−9.00
18013	23.14	21.95	20.92	20.12	19.71	19.73	19.33	−9.00	−9.00	−9.00
11700	22.99	21.84	20.81	19.98	19.53	19.57	19.20	−9.00	−9.00	−9.00
18023	22.39	21.01	19.72	18.76	18.19	18.22	17.78	−9.00	−9.00	−9.00
24007	22.70	21.57	20.57	19.66	19.10	19.17	18.88	−9.00	−9.00	−9.00
24012	22.33	21.29	20.21	19.30	18.79	18.74	18.39	17.94	17.50	17.36
18700	21.89	20.51	19.15	18.23	17.73	17.73	17.32	16.83	16.60	16.50
24015	21.77	20.99	20.05	19.32	18.91	18.86	18.61	18.24	17.97	17.92
18030	23.43	22.00	20.83	19.92	19.47	19.48	19.08	18.51	18.20	18.04
24016	21.08	20.01	18.87	17.97	17.47	17.47	17.11	16.62	16.42	16.32
18033	20.94	20.31	19.55	18.90	18.49	18.54	18.22	17.74	17.54	17.33
18072	21.91	20.43	19.13	18.19	17.65	17.75	17.22	16.81	16.61	16.51
24027	21.99	20.54	19.18	18.22	17.66	17.69	17.26	16.70	16.42	16.29
24030	22.24	21.48	20.59	19.89	19.50	19.49	19.18	19.03	18.73	18.76
18041	21.64	20.12	18.75	17.78	17.26	17.31	16.89	16.41	16.23	16.07
18071	21.92	20.75	19.60	18.75	18.26	18.35	17.90	17.33	17.01	16.95
18042	22.02	20.54	19.21	18.24	17.75	17.80	17.39	16.85	16.63	16.49
24111	21.27	20.74	20.10	19.61	19.52	19.56	19.22	18.93	18.82	18.67
18045	20.85	20.41	19.86	19.44	19.34	19.40	19.18	18.94	18.77	18.93
18047	21.15	20.64	20.01	19.51	19.29	19.36	19.10	18.80	18.72	18.63
18048	20.73	20.10	19.37	18.78	18.39	18.44	18.13	17.74	17.49	17.44
24701	22.33	20.99	19.66	18.70	18.24	18.26	17.91	17.26	17.08	16.96
18702	21.05	20.41	19.67	19.03	18.71	18.72	18.47	18.13	18.01	17.97
24033	22.04	20.61	19.27	18.31	17.79	17.82	17.47	16.87	16.61	16.50
18703	22.25	20.88	19.60	18.69	18.20	18.24	17.88	17.29	17.05	17.00
05012	21.96	20.77	19.68	18.81	18.30	18.32	17.87	−9.00	−9.00	−9.00
18070	22.23	21.70	21.06	20.48	20.39	20.42	20.10	19.88	19.56	19.47
24115	22.47	21.00	19.73	18.80	18.35	18.32	17.97	17.56	17.36	17.20
18056	21.90	21.02	20.03	19.25	18.80	18.88	18.48	17.92	17.75	17.45

Table 3—Continued

Name	U	B	V	R	I	8010	9170	J	H	K
18057	21.85	20.55	19.28	18.34	17.81	17.89	17.41	16.96	16.72	16.58
18300	21.68	21.10	20.29	19.76	19.51	19.65	19.45	18.96	18.82	18.80
18060	21.42	20.58	19.58	18.80	18.40	18.48	18.12	17.58	17.42	17.17
18061	21.60	20.51	19.38	18.51	18.05	18.07	17.72	17.33	17.09	16.93
18062	22.04	21.36	20.56	19.90	19.65	19.59	19.34	18.71	18.40	18.06
25001	21.69	20.47	19.25	18.38	17.87	17.90	17.53	17.06	16.77	16.64
00002	22.09	20.55	19.25	18.31	17.82	17.88	17.53	17.15	16.81	16.68
00600	22.57	21.77	20.86	20.11	19.73	19.80	19.46	18.76	18.85	18.56
12004	21.87	21.19	20.50	19.86	19.50	19.44	19.26	−9.00	−9.00	−9.00
00007	20.79	20.25	19.62	19.05	18.73	18.76	18.24	18.33	18.14	17.98
12007	21.93	21.01	20.03	19.26	18.80	18.84	18.46	18.09	17.75	17.71
25100	21.08	20.39	19.58	18.93	18.50	18.49	18.22	−9.00	−9.00	−9.00
25010	23.10	22.12	21.08	20.23	19.70	19.87	19.47	18.77	18.30	18.04
00700	22.68	21.79	20.82	19.95	19.61	19.66	19.18	18.86	18.64	18.60
00014	22.77	21.73	20.57	19.59	19.26	19.23	18.83	18.09	17.73	17.57
25702	21.32	20.28	19.12	18.27	17.72	17.78	17.42	−9.00	−9.00	−9.00
00104	22.31	20.91	19.62	18.72	18.24	18.28	17.89	17.50	17.20	17.24
00020	21.38	20.63	19.84	19.14	18.72	18.83	18.51	17.89	17.66	17.65
00022	21.83	21.22	20.42	19.77	19.57	19.53	19.33	18.54	18.25	18.08
25015	22.35	21.39	20.37	19.59	19.11	19.03	18.72	−9.00	−9.00	−9.00
00026	22.65	21.97	20.92	19.93	19.30	19.35	18.94	18.30	17.93	17.82
00027	21.40	20.49	19.47	18.63	18.20	18.18	17.84	17.26	16.98	16.85
00028	22.83	21.33	20.03	19.07	18.62	18.61	18.21	17.69	17.42	17.39
12027	21.80	20.52	19.33	18.46	17.99	17.96	17.59	−9.00	−9.00	−9.00
00031	22.19	21.46	20.57	19.85	19.49	19.68	19.26	18.69	18.41	18.36
00034	21.68	20.27	18.99	18.07	17.56	17.62	17.23	16.68	16.38	16.32
00039	21.42	19.96	18.64	17.70	17.16	17.23	16.80	16.24	15.95	15.90
00201	21.96	21.30	20.52	19.87	19.61	19.64	19.34	18.74	18.55	18.57
12033	21.05	20.19	19.23	18.45	18.05	17.95	17.67	17.15	16.84	16.79
00047	20.76	20.20	19.55	18.92	18.67	18.67	18.40	17.80	17.47	17.38
00703	23.08	21.70	20.51	19.54	19.30	19.31	18.94	18.25	17.98	17.94

Table 3—Continued

Name	U	B	V	R	I	8010	9170	J	H	K
00051	22.04	21.34	20.57	19.94	19.61	19.74	19.38	18.84	18.78	18.80
00057	21.20	19.72	18.40	17.42	16.90	16.94	16.54	16.00	15.69	15.66
00105	21.25	19.78	18.42	17.47	16.92	16.99	16.54	16.00	15.70	15.65
00106	21.74	20.30	18.90	18.01	17.46	17.49	17.11	16.75	16.43	16.44
00060	21.29	20.44	19.50	18.74	18.31	18.34	17.99	17.48	17.23	17.13
00701	22.36	21.19	19.94	18.99	18.55	18.60	18.16	17.49	17.19	17.13
25701	21.86	20.50	19.25	18.35	17.84	17.83	17.53	17.11	16.86	16.70
12068	22.34	21.77	20.94	20.13	19.93	19.96	20.20	19.30	19.15	18.77
00077	22.81	21.87	20.93	20.15	20.09	19.97	19.64	18.93	18.55	18.29
06008	21.02	19.62	18.35	17.46	16.91	16.95	16.48	−9.00	−9.00	−9.00
12058	23.21	21.85	20.64	19.68	19.18	19.10	18.81	18.33	17.73	18.20
12100	23.30	22.18	21.06	20.20	19.78	19.72	19.56	18.94	18.40	18.19
00084	23.57	22.53	21.63	20.84	20.44	20.44	20.19	19.46	19.06	18.95
00085	21.83	21.16	20.39	19.78	19.58	19.57	19.30	18.83	18.63	18.63
12702	20.89	20.21	19.48	18.83	18.44	18.38	18.20	−9.00	−9.00	−9.00
00089	22.20	20.91	19.47	18.73	18.25	18.18	17.85	17.30	17.05	17.03
00704	21.74	20.68	19.52	18.60	18.13	18.19	17.79	17.21	16.92	16.94
12061	22.54	21.65	20.68	19.93	19.45	19.49	19.15	-9.00	-9.00	-9.00
00705	22.51	21.18	19.96	19.04	18.61	18.58	18.23	17.63	17.33	17.35
00098	22.30	21.25	20.16	19.29	18.84	18.77	18.43	17.81	17.52	17.43
13700	22.08	21.30	20.37	19.61	19.21	19.25	18.86	18.39	18.05	18.02
19011	22.60	21.51	20.38	19.46	18.97	18.88	18.58	17.83	17.42	17.35
13003	21.89	21.02	20.06	19.25	18.78	18.78	18.40	−9.00	−9.00	−9.00
13004	22.09	21.17	20.17	19.31	18.68	18.70	18.26	−9.00	−9.00	−9.00
13008	21.67	20.89	20.01	19.27	18.91	18.87	18.58	18.02	17.77	17.64
13015	21.89	20.45	19.15	18.19	17.69	17.69	17.28	17.03	16.75	16.58
13702	22.33	20.98	19.75	18.82	18.30	18.31	17.89	−9.00	−9.00	−9.00
19061	21.34	20.68	20.00	19.42	19.05	18.88	18.80	−9.00	−9.00	−9.00

Table 4. A2125 Member Physical Parameters

Name	Size kpc	$\log(L_{20cm})$ W/Hz	Proj Dist Mpc	M_R mag	Spec T.	Age Gyrs	A_V mag	z
17017	<8.4	22.40	3.7	-22.1	1	2.6	0.8	0.2475
23009	15.7	22.70	3.43	-21.6	2	5.5	1.2	0.2575
23016	95.8	25.00	2.93	-21.8	2	6.5	0.6	0.2449
18013	<5.0	22.41	2.38	-20.5	1	2.0	0.2	0.2449e
11700	<9.6	21.95	2.40	-20.7	2	6.5	0.0	0.2442e
18023	<4.6	22.51	2.12	-21.9	1	2.0	1.0	0.2448
24007	3.8	22.79	3.00	-21.2	2	5.5	0.4	0.2468e
24012	6.1	22.46	2.48	-21.3	3	9.5	0.6	0.2445e
18700	<6.9	21.82	1.74	-22.4	2	9.5	0.2	0.2458
24015	10.0	22.28	2.00	-21.4	2	4.5	0.2	0.2408e
18030	<3.4	22.15	1.76	-20.8	1	1.7	0.8	0.2482e
24016	13.8	22.66	2.07	-22.6	3	11.5	0.2	0.2458
18033	7.7	22.77	1.79	-21.8	5	11.5	0.4	0.2458e
18072	379.2	24.25	1.54	-22.4	1	7.5	0.2	0.2459
24027	17.6	23.21	1.83	-22.5	1	4.5	0.6	0.2425
24030	7.3	22.14	1.81	-20.8	2	4.5	0.0	0.2436e
18041	8.8	22.82	1.54	-22.9	1	11.5	0.0	0.2455
18701	32.6	22.40	1.32	-21.8	2	5.5	0.6	0.2477
18042	<2.7	22.74	1.50	-22.4	2	9.5	0.2	0.2458
24111	21.1	22.26	1.74	-20.8	2	1.7	0.4	0.2460e
18045	6.1	22.02	1.50	-21.1	1	0.1	0.8	0.2458e
18047	8.4	22.23	1.28	-21.1	4	5.5	0.0	0.2433e
18048	6.5	22.75	1.55	-21.9	5	11.5	0.2	0.2455e
24701	<7.3	21.83	1.60	-22.0	2	8.5	0.2	0.2559
18702	10.3	21.80	1.51	-21.6	3	6.5	0.0	0.2443e
24033	<7.3	21.91	1.60	-22.4	1	5.5	0.4	0.2565
18703	9.6	21.75	1.05	-22.0	2	8.5	0.2	0.2500
05012	6.9	22.86	3.06	-21.8	2	5.5	0.6	0.2573
18070	5.7	21.93	0.98	-20.0	3	3.5	0.2	0.2475e
24115	<5.0	21.98	2.04	-21.8	1	8.5	0.0	0.2421

Table 4—Continued

Name	Size kpc	$\log(L_{20cm})$ W/Hz	Proj Dist Mpc	M_R mag	Spec T.	Age Gyrs	A_V mag	z
18056	3.4	22.52	1.19	-21.3	3	7.5	0.6	0.2456e
18057	4.6	22.40	1.09	-22.2	2	7.5	0.4	0.2494e
18300	<7.7	21.69	1.15	-21.0	2	2.6	0.2	0.2458e
18060	10.0	22.52	1.14	-21.9	2	4.5	0.4	0.2474e
18061	11.9	22.22	0.95	-22.2	3	11.5	0.0	0.2430
18062	7.3	22.40	0.91	-20.7	3	1.0	1.6	0.2444e
25001	18.8	22.38	1.68	-22.3	1	2.0	0.6	0.2530e
00002	<3.4	22.42	0.89	-22.4	1	8.5	0.0	0.2548
00600	<5.7	21.82	1.07	-20.6	4	10.5	0.2	0.2423e
12004	6.5	22.06	1.78	-20.9	4	9.5	0.0	0.2381e
00007	10.3	22.40	0.92	-21.6	3	5.5	0.0	0.2462e
12007	11.9	22.10	1.05	-21.4	2	4.5	0.4	0.2429e
25100	18.4	22.55	2.35	-21.8	5	10.5	0.6	0.2521e
25010	<2.7	22.65	1.31	-20.5	2	2.3	1.6	0.2558
00700	8.0	21.83	0.59	-20.6	3	9.5	0.0	0.2469
00014	21.1	22.49	0.81	-20.9	2	4.5	1.0	0.2423
25702	42.1	22.85	2.19	-22.4	3	10.5	0.4	0.2561
00104	95.8	24.43	0.76	-22.0	1	7.5	0.0	0.2433
00020	17.2	22.39	0.57	-21.6	4	8.5	0.4	0.2419e
00022	5.7	22.50	0.84	-20.8	2	0.7	1.6	0.2588e
25015	<3.8	22.41	2.16	-21.1	2	4.5	0.6	0.2508e
00026	<2.7	22.55	1.01	-20.9	4	10.5	1.0	0.2484e
00027	3.1	22.72	0.50	-22.1	2	4.5	0.6	0.2460e
00028	<4.2	21.97	0.44	-21.5	1	7.5	0.2	0.2486
12027	11.9	22.71	2.18	-22.2	1	2.0	0.6	0.2463
00031	10.3	22.21	0.40	-20.7	2	2.3	1.0	0.2545e
00034	<3.8	21.85	0.68	-22.6	1	3.5	0.4	0.2395
00039	<3.1	22.54	0.30	-23.0	1	5.5	0.4	0.2457
00201	<20.7	22.09	0.57	-20.6	2	2.6	0.6	0.2454e
12033	16.1	22.32	0.78	-22.1	4	11.5	0.4	0.2406e

Table 4—Continued

Name	Size kpc	$\log(L_{20cm})$ W/Hz	Proj Dist Mpc	M_R mag	Spec T.	Age Gyrs	A_V mag	z
00047	53.6	24.59	0.14	-21.7	8	3.5	1.0	0.2528e
00703	24.1	22.42	0.17	-20.9	1	1.4	0.8	0.2494
00051	9.6	21.96	0.65	-20.6	4	9.5	0.0	0.2473e
00057	10.7	23.69	0.03	-23.3	1	5.5	0.4	0.2518
00105	15.3	23.06	0.03	-23.1	1	7.5	0.4	0.2470
00106	88.1	24.42	0.02	-22.7	1	9.5	0.0	0.2466
00060	11.1	22.27	0.34	-22.0	3	7.5	0.4	0.2422e
00701	<8.8	21.61	0.13	-21.6	3	11.5	0.4	0.2480
25701	<5.0	21.74	1.47	-22.4	1	4.5	0.2	0.2454
12068	<5.4	22.05	1.10	-20.5	2	2.3	0.6	0.2484e
00077	6.1	22.35	0.44	-20.2	1	0.2	1.8	0.2516e
06008	<4.6	22.77	3.06	-23.1	1	2.3	0.8	0.2369
12058	<3.4	22.40	1.43	-21.0	1	5.5	0.2	0.2514
12100	11.1	22.24	1.43	-20.5	2	4.5	0.8	0.2488e
00084	4.6	22.14	0.52	-19.8	2	2.6	1.2	0.2397e
00085	14.2	22.39	0.67	-20.9	2	2.6	0.4	0.2517
12702	<11.9	22.04	2.30	-21.9	5	11.5	0.4	0.2398e
00089	5.4	22.41	0.57	-21.8	2	8.5	0.2	0.2518
00704	31.0	22.70	0.64	-22.0	3	11.5	0.2	0.2547
12061	<3.4	22.40	2.06	-20.9	2	4.5	0.4	0.2492e
00705	35.6	22.51	0.78	-21.6	1	2.3	0.6	0.2444
00098	<3.4	22.10	0.99	-21.3	2	4.5	0.8	0.2473e
13700	<5.4	21.77	1.12	-20.9	4	10.5	0.4	0.2534
19011	17.6	22.07	0.94	-21.2	2	4.5	1.0	0.2412e
13003	10.7	22.48	2.36	-21.4	4	9.5	0.8	0.2468e
13004	16.5	22.89	2.31	-21.5	5	7.5	1.8	0.2458e
13008	12.3	22.18	1.29	-21.4	4	9.5	0.4	0.2501e
13015	5.0	22.59	1.59	-22.4	1	9.5	0.0	0.2473
13702	25.3	22.58	2.18	-21.8	1	2.0	0.8	0.2390
19061	7.7	22.34	2.29	-21.4	5	11.5	0.2	0.2394e

Table 4—Continued

Name	Size kpc	$\log(L_{20cm})$ W/Hz	Proj Dist Mpc	M_R mag	Spec T.	Age Gyrs	A_V mag	z

Table 5. A2125 Radio Members with X-ray Detections

Name	RA(2000.0)	Dec(2000.0)	X Name	X_{lum}	R_{lum}	Abs mag	z
24016	15 39 52.60	66 09 54.1	X014	41.9	22.66	-22.6	0.2458
24027	15 40 05.34	66 10 12.9	X022	41.7	23.21	-22.5	0.2425
18041	15 40 09.11	66 12 17.1	X025	41.7	22.82	-22.9	0.2455
24701	15 40 16.49	66 10 39.7	X033	41.7	21.83	-22.0	0.2559
00034	15 41 00.37	66 19 02.8	X063	41.6	21.85	-22.6	0.2395
00039	15 41 01.94	66 16 26.5	X065	42.1	22.54	-23.0	0.2457
00047	15 41 09.73	66 15 44.5	X068	41.7	24.59	-21.7	0.2528e
00704	15 41 43.39	66 14 19.1	X087	41.7	22.70	-22.0	0.2547

Note. — col 1: radio source name, col 2-3 R.A., Dec (2000.0), col 4: X-ray source name (Wang, Owen & Ledlow 2004), col 5: log $0.5 - 8.0$ keV X-ray luminosity, col 6: log 20cm radio luminosity, col 7: absolute R magnitude; col 8: redshift (Miller et al. 2004)

Table 6. A2125 Radio Members with Faint X-ray Detections.

Name	RA(2000.0)	Dec(2000.0)	X_{lum}	X band	X class	R_{lum}	Abs mag	z
18030	15 39 52.47	66 13 18.5	41.1	S	d	22.15	-20.8	0.2482e
18700	15 39 50.14	66 14 54.7	41.4	B	p	21.82	-22.4	0.2458
18701	15 40 10.34	66 15 46.2	40.9	S	p	22.40	-21.8	0.2477
18045	15 40 13.98	66 11 50.7	41.3	B	e	22.02	-21.1	0.2458e
18048	15 40 15.84	66 11 09.9	40.9	S	?	22.75	-21.9	0.2455e
18702	15 40 17.14	66 11 15.9	41.2	B	?	21.80	-21.6	0.2443e
24033	15 40 21.42	66 10 12.1	41.3	B	e	21.91	-22.4	0.2565
00022	15 40 52.63	66 12 30.4	40.8	B	p	22.50	-20.8	0.2588e
00026	15 40 54.49	66 11 27.4	41.3	S	p	22.55	-20.9	0.2484e
00027	15 40 54.67	66 17 15.7	41.3	B	p	22.72	-22.1	0.2460e
00051	15 41 11.59	66 12 47.9	40.9	S	?	21.96	-20.6	0.2473e
00057	15 41 14.37	66 15 57.1	41.6	B	d	23.69	-23.3	0.2518

Note. — col 1: radio source name, col 2-3 R.A., Dec (2000.0), col 4: log $0.5 - 8.0$ keV X-ray luminosity, col 5: log 20cm radio luminosity, col 6: X-ray band in which detection was made: S:soft(0.5–2.0 keV), B:both(0.5–8.0 keV), col 7: detection class: d: diffuse feature, e: clearly extended, p: point-like, ?: too faint to make a classification, col 8: absolute R magnitude, col 9: redshift (Miller et al. 2004)

Table 7. A2125 Members with X-ray Detections and no Radio Detection

Name	RA(2000.0)	Dec(2000.0)	X_{lum}	z
X064	15 41 02.01	66 17 20.9	42.5	0.2554
X072	15 41 17.32	66 19 23.7	41.9	0.2463

Note. — col 1: X-ray source name(Wang, Owen & Ledlow 2004) , col 2-3 R.A., Dec (2000.0), col 4: log 0.5 – 8.0 keV col 5: redshift (Miller et al. 2004)

Table 8. A2125 Star-formation Index

Name	L_{20cm}	Align	Mag	Emis	Age	Dust	Total
17017	0.5	0.0	0.0	0.0	0.5	0.5	1.5
23009	0.0	1.0	0.0	0.0	0.0	1.0	2.0
23016	0.0	0.0	0.0	0.0	0.5	0.0	0.5
18013	0.5	0.0	0.5	1.0	0.5	0.0	2.5
11700	0.5	0.0	0.5	1.0	0.0	0.0	2.0
18023	0.5	0.0	0.0	0.0	0.5	1.0	2.0
24007	0.0	1.0	0.0	1.0	0.0	0.0	2.0
24012	0.5	1.0	0.0	1.0	0.0	0.5	3.0
18700	0.5	0.0	0.0	0.0	0.0	0.0	0.5
24015	0.5	1.0	0.0	1.0	0.5	0.0	3.0
18030	0.5	0.0	0.5	1.0	0.5	0.5	3.0
24016	0.5	0.0	0.0	0.0	0.0	0.0	0.5
18033	0.0	1.0	0.0	1.0	0.0	0.0	2.0
18072	0.0	0.0	0.0	0.0	0.0	0.0	0.0
24027	0.0	0.0	0.0	0.0	0.5	0.5	1.0
24030	0.5	1.0	0.5	1.0	0.5	0.0	3.5
18041	0.0	0.0	0.0	0.0	0.0	0.0	0.0
18701	0.5	1.0	0.0	0.0	0.0	0.5	2.0
18042	0.0	0.0	0.0	0.0	0.0	0.0	0.0
24111	0.5	1.0	0.5	1.0	0.5	0.0	3.5
18045	0.5	0.0	0.0	1.0	1.0	0.5	3.0
18047	0.5	1.0	0.0	1.0	0.0	0.0	2.5
18048	0.0	1.0	0.0	1.0	0.0	0.0	2.0
24701	0.5	0.0	0.0	0.0	0.0	0.0	0.5
18702	0.5	1.0	0.0	1.0	0.0	0.0	2.5
24033	0.5	0.0	0.0	0.0	0.0	0.0	0.5
18703	0.5	1.0	0.0	0.0	0.0	0.0	1.5
05012	0.0	1.0	0.0	0.0	0.0	0.5	1.5
18070	0.5	0.0	0.5	1.0	0.5	0.0	2.5
24115	0.5	0.0	0.0	0.0	0.0	0.0	0.5

Table 8—Continued

Name	L_{20cm}	Align	Mag	Emis	Age	Dust	Total
18056	0.5	1.0	0.0	1.0	0.0	0.0	2.5
18057	0.5	1.0	0.0	1.0	0.0	0.0	2.5
18300	0.5	0.0	0.5	1.0	0.5	0.0	2.5
18060	0.5	1.0	0.0	1.0	0.5	0.0	3.0
18061	0.5	0.0	0.0	0.0	0.0	0.0	0.5
18062	0.5	0.0	0.5	1.0	1.0	1.0	4.0
25001	0.5	0.0	0.0	1.0	0.5	0.5	2.5
00002	0.5	0.0	0.0	0.0	0.0	0.0	0.5
00600	0.5	0.0	0.5	1.0	0.0	0.0	2.0
12004	0.5	1.0	0.5	1.0	0.0	0.0	3.0
00007	0.5	1.0	0.0	1.0	0.0	0.0	2.5
12007	0.5	1.0	0.0	1.0	0.5	0.0	3.0
25100	0.5	0.0	0.0	1.0	0.0	0.5	2.0
25010	0.5	0.0	0.5	0.0	0.5	1.0	2.5
00700	0.5	0.0	0.5	0.0	0.0	0.0	1.0
00014	0.5	1.0	0.5	0.0	0.5	1.0	3.5
25702	0.0	0.0	0.0	0.0	0.0	0.0	0.0
00104	0.0	0.0	0.0	0.0	0.0	0.0	0.0
00020	0.5	1.0	0.0	1.0	0.0	0.0	2.5
00022	0.5	0.0	0.5	1.0	1.0	1.0	4.0
25015	0.5	0.0	0.0	1.0	0.5	0.5	2.5
00026	0.5	0.0	0.5	1.0	0.0	1.0	3.0
00027	0.0	0.0	0.0	1.0	0.5	0.5	2.0
00028	0.5	0.0	0.0	0.0	0.0	0.0	0.5
12027	0.0	1.0	0.0	0.0	0.5	0.5	2.0
00031	0.5	1.0	0.5	1.0	0.5	1.0	4.5
00034	0.0	0.0	0.0	0.0	0.5	0.0	1.0
00039	0.5	0.0	0.0	0.0	0.0	0.0	0.5
00201	0.5	0.0	0.5	1.0	0.5	0.5	3.0
12033	0.5	1.0	0.0	1.0	0.0	0.0	2.5
00047	0.0	1.0	0.0	1.0	0.5	1.0	3.5

Table 8—Continued

Name	L_{20cm}	Align	Mag	Emis	Age	Dust	Total
00703	0.5	0.0	0.5	0.0	0.5	0.5	2.0
00051	0.5	0.0	0.5	1.0	0.0	0.0	2.0
00057	0.0	0.0	0.0	0.0	0.0	0.0	0.0
00105	0.0	0.0	0.0	0.0	0.0	0.0	0.0
00106	0.0	0.0	0.0	0.0	0.0	0.0	0.0
00060	0.5	1.0	0.0	1.0	0.0	0.0	2.5
00701	0.5	0.0	0.0	0.0	0.0	0.0	0.5
25701	0.5	0.0	0.0	0.0	0.5	0.0	1.0
12068	0.5	0.0	0.5	1.0	0.5	0.5	3.0
00077	0.5	1.0	0.5	1.0	1.0	0.5	5.0
06008	0.0	0.0	0.0	0.0	0.5	0.5	1.0
12058	0.5	0.0	0.0	0.0	0.0	0.0	0.5
12100	0.5	0.0	0.5	1.0	0.5	0.5	3.0
00084	0.5	1.0	0.5	1.0	0.5	1.0	4.5
00085	0.5	0.0	0.5	0.0	0.5	0.0	1.5
12702	0.5	0.0	0.0	1.0	0.0	0.0	1.5
00089	0.5	0.0	0.0	0.0	0.0	0.0	0.5
00704	0.0	0.0	0.0	0.0	0.0	0.0	0.0
12061	0.5	0.0	0.5	1.0	0.5	0.0	2.5
00705	0.5	0.0	0.0	0.0	0.5	0.5	1.5
00098	0.5	0.0	0.0	1.0	0.5	0.5	2.5
13700	0.5	0.0	0.5	0.0	0.0	0.0	1.0
19011	0.5	1.0	0.0	1.0	0.5	1.0	4.0
13003	0.5	1.0	0.0	1.0	0.0	0.5	3.0
13004	0.0	1.0	0.0	1.0	0.0	1.0	3.0
13008	0.5	1.0	0.0	1.0	0.0	0.0	2.5
13015	0.5	0.0	0.0	0.0	0.0	0.0	0.5
13702	0.5	1.0	0.0	0.0	0.5	0.5	2.5
19061	0.5	1.0	0.0	0.0	0.0	0.0	1.5